Late Neoproterozoic to early Cambrian high-grade metamorphism from Mikir Hills (Assam-Meghalaya gneissic Complex, northeast India): Implications for eastern Gondwana assembly

Rahul Nag, H. Hrushikesh, Nathan Cogné, N. Prabhakar

Journal Pre-proofs

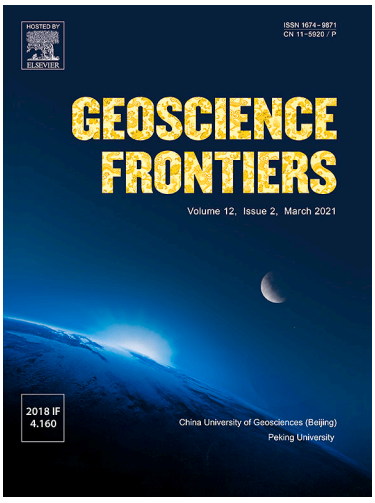

Research Paper

Late Neoproterozoic to early Cambrian high-grade metamorphism from Mikir Hills (Assam-Meghalaya gneissic Complex, northeast India): Implications foreastern Gondwana assembly

Rahul Nag, H. Hrushikesh, Nathan Cogné, N. Prabhakar

PII: S1674-9871(24)00074-4
DOI: https://doi.org/10.1016/j.gsf.2024.101850
Reference: GSF 101850

To appear in: *Geoscience Frontiers*

Received Date: 31 August 2023
Revised Date: 2 February 2024
Accepted Date: 30 April 2024

Please cite this article as: R. Nag, H. Hrushikesh, N. Cogné, N. Prabhakar, Late Neoproterozoic to early Cambrian high-grade metamorphism from Mikir Hills (Assam-Meghalaya gneissic Complex, northeast India): Implications foreastern Gondwana assembly, *Geoscience Frontiers* (2024), doi: https://doi.org/10.1016/j.gsf.2024.101850

Research Paper

Late Neoproterozoic to Early Cambrian high-grade metamorphism from Mikir Hills (Assam-Meghalaya Gneissic Complex, northeast India): Implications for eastern Gondwana assembly

Rahul Nag[a], H. Hrushikesh[b], Nathan Cogné[c], N. Prabhakar[a,*]

*Corresponding author: prabhakarnaraga@iitb.ac.in; prabhakarnaraga@gmail.com

[a] Department of Earth Sciences, Indian Institute of Technology Bombay, Powai, Mumbai, Maharastra-400076, India

[b] Geological Survey of India, Northeastern Region, Guwahati, Assam-781005, India

[c] Géosciences Rennes, UMR6118, CNRS Université de Rennes, France

Abstract

Mikir Hills region, which represents the eastern segment of the Assam-Meghalaya Gneissic Complex (AMGC) in northeast India, constitutes part of the Eastern Gondwana. The Mikir Hills preserves multiple metamorphic and magmatic events ranging from Early Mesoproterozoic to Early Cambrian. Out of these events, documenting the late Neoproterozoic to early Cambrian tectonothermal events is helpful in correlating the continental blocks of Eastern Gondwana. We present an integrated study involving field relations, petrology, *P–T* history and zircon-monazite geochronology of hitherto poorly studied pelitic and quartzo-feldspathic gneisses from the Mikir Hills region. These gneisses have experienced at least three deformation events (D_1, D_2 and D_3) with dominant foliation indicated by ENE–WSW striking and shallow-moderately dipping (< 40°) S_2 gneissic foliation. The peak metamorphism in pelitic and quartzo-feldspathic gneisses is characterized by garnet(core)–K-feldspar–sillimanite–plagioclase–biotite–rutile–quartz–ilmenite–melt and garnet–plagioclase–K-feldspar–biotite–quartz–ilmenite–melt assemblages, respectively. The application of thermobarometric methods constrains the peak *P–T* conditions of 7.5–8.4 kbar at 674–778 °C and 6.7–7.4 kbar at 601–618 °C for pelitic and quartzo-feldspathic gneisses, respectively. These results are consistent with the values estimated using phase equilibria modelling and melt reintegration approach. The results of pseudosection modelling suggests a clockwise *P–T* path for pelitic gneisses involving migmatisation during peak metamorphism followed by near isothermal decompression from 8.0–8.6 kbar at 768–780 °C to

4.0–5.0 kbar at 720–765 °C. In contrast, quartzo-feldspathic gneisses preserved slightly lower peak *P–T* conditions at 3.8–4.6 kbar and 590–650 °C. The U–Pb zircon dating of migmatised pelitic and quartzo-feldspathic gneisses yielded concordant ages of 1647 ± 11 Ma and 1590 ± 7 Ma, respectively. These dates represent the inherited igneous protolith components, possibly equivalent to the Mesoproterozoic granulite facies metamorphism in the western AMGC. The rarely preserved cores of monazite in pelitic gneisses yielded an older population of 1058 ± 35 Ma, most likely representing a weak tectonic imprint associated with the amalgamation of India with Western Australia and East Antarctica in the Rodinia assembly. However, the majority of monazite grains in pelitic and quartzo-feldspathic gneisses show high Th/U ratios with ages between 496 ± 7 Ma and 467 ± 16 Ma, indicating the timing of migmatisation that is contemporary with voluminous ~500 Ma granite magmatism in and around the Mikir Hills. The similarities in *P–T–t* histories estimated in this study (eastern AMGC) and those obtained from the Sonapahar-Umpretha region (central AMGC) confirm that these domains experienced common tectonometamorphic history during Pan-African orogeny. The dominance of Late Neoproterozoic migmatisation and magmatism in the Mikir Hills region indicate that the eastern AMGC represent an active convergent margin with Western Australia and East Antarctica and evolved as a hot orogen during the assembly of Western and Eastern Gondwana continental fragments.

Keywords: Gondwana; Assam-Meghalaya Gneissic Complex; migmatisation; Neoproterozoic; Geochronology; *P–T–t* history

Handling Editor: Vinod Samuel

1. Introduction

The assembly of the Gondwana supercontinent was mainly governed by continent-continent collision, high-grade metamorphism, crustal anatexis and post-collisional magmatism, leading to the development of various Pan-African orogenic belts (Fitzsimons, 2003; Meert, 2003; Collins and Pisarevsky, 2005; Santosh et al., 2017; Boger et al., 2019; Mulder et al., 2019). The formation of Gondwana assembly is associated with two orogenic belts – the East African orogen and the Kuunga orogen. The N–S striking East African orogen (~750–620 Ma) is formed due to the closure of Mozambique Ocean, resulting in the collision between Sahara–Kalahari–Congo crustal block to the west and India–Western Australia–East Antarctica to the east (Stern, 1994; Fritz et al., 2013). However, oceans still existed between southern and eastern India, Congo Craton, Kalahari Craton, Western Australia and East Antarctica, which were subsequently closed by ~500 Ma (e.g., Meert, 2003; Collins and Pisarevsky, 2005). This ocean closure led to the development of the Kuunga orogen (~635–488 Ma), marking the youngest orogenic event in the Gondwana assembly (Fig. 1a; Meert, 2003). This orogeny has resulted in high-grade metamorphism along the margins of Congo and Kalahari cratons (557–555 Ma; 650–875 °C at 6.7–11.0 kbar; Kuribara et al., 2019) and HT to UHT metamorphism in Androyan Group of

Madagascar (~560–530 Ma; 950–1000 °C at 8–11 kbar; Jöns and Schenk, 2011). Similar high-grade metamorphic events have been reported throughout the Madurai, Trivandram, Salem and Nagercoil blocks in Southern India (~550–500 Ma; 940–1150 °C at 7–11 kbar; Plavsa et al., 2015), Highland Complex of Sri Lanka (~580–530 Ma; 925–1150 °C at 9.0–12.5 kbar; Santosh et al., 2014; Dharmapriya et al., 2015) and Prydz bay belt of Antarctica (~570–500 Ma; 800–1000 °C at 9.0–13.5 kbar; Merdith et al., 2017; Spreitzer et al., 2021). Along the eastern margin of India, the evidence of the Kuunga orogeny have been locally preserved in Eastern Ghats (~550–500 Ma; Bose and Dasgupta, 2018). However, the studies reconstructing the large-scale tectonism associated with the Kuunga orogeny along the northeastern margin of India are limited and mostly focused on tectonothermal evolution of pelitic gneisses (Chatterjee et al., 2007, 2011; Dwivedi et al., 2020) and geochemical and geochronological studies of magmatic rocks (Yin et al., 2010; Majumdar and Dutta, 2016; Kumar et al., 2017) from specific locations of the Assam-Meghalaya Gneissic Complex (NE India).

The Assam-Meghalaya Gneissic Complex (AMGC), located on the northeastern margin of the Great Indian landmass, plausibly juxtaposed with the East Antarctica and Western Australia shields during the East Gondwana amalgamation (Fig. 1a; Chatterjee et al., 2007, 2011). The AMGC has been regarded as one of the key crustal domain of East Gondwana due to its abundant Neoproterozoic lithologies, which are critical for reconstructing the magmatic-metamorphic evolution of Pan-African orogens. Over the past two decades, most of the geological studies were focused on the western (Garo-Goalpara Hills; Chatterjee et al., 2007, 2011; Chatterjee, 2017) and central (Sonapahar-Umpretha-Umling; Chatterjee et al., 2011; Dwivedi et al., 2020) parts of the AMGC (Fig. 1b). These studies identified two high-grade (upper amphibolite to granulite facies) metamorphic events during 1672–1596 Ma and 496–478 Ma (Chatterjee et al., 2007, 2011; Dwivedi et al., 2020, 2023) and a magmatic event at ~1129–1039 Ma (Yin et al., 2010). Based on metamorphic history and the dominance of ~500 Ma tectonism, the western extent of Pan-African orogeny in northeast India was identified between the Garo-Goalpara Hills and Sonapahar areas of the central AMGC (Chatterjee et al., 2007). They argue that this suture is continuous with the Prydz Bay belt in East Antarctica. However, the characteristics and extension of Pan-African orogeny and its significance in the eastern parts of the AMGC, particularly in the Mikir Hills region (Fig. 1b), have been poorly documented. For example, U–Pb zircon dating of granitoids from the western and central parts of the Mikir Hills yielded an age range of ~529–515 Ma (Majumdar and Dutta, 2016; Kumar et al., 2017). In contrast, the easternmost parts of the Mikir Hills are dominated by Late Paleoproterozoic to Early Mesoproterozoic granitoids (1644–1550 Ma; Gogoi et al., 2019) and gneisses (1430 ± 10 Ma; Kumar et al., 2017). According to Majumdar and Dutta (2016), the emplacement of ~500 Ma granitoids represent a post-collisional magmatic event associated with the assembly of Western and Eastern Gondwana. Although the gamut of these geological and geochronological results indicates that the eastern extension of Pan-African orogeny extends further within Mikir Hills region, the tectonothermal history of gneisses and associated lithologies of Mikir Hills in the context of eastern Gondwana assembly has not been investigated in detail.

This study aims to fill the gap by investigating the metamorphic *P–T–t* history of migmatised pelitic and quartzo-feldspathic gneisses from the Mikir Hills region (eastern AMGC; Fig. 1b), an important crustal domain linking northeast India with other dismembered units in the eastern Gondwana assembly. We combine the results of field relations, petrography, mineral paragenesis, phase equilibrium modelling and zircon-monazite geochronology to provide a

detailed account of the tectonothermal evolution of Mikir Hills within the framework of Eastern Gondwana assembly. The new results can provide valuable insights into the spatial and temporal distribution of Kuunga orogeny and have implications for correlating global Pan-African orogens.

2. Geological background

The ~300 km long and ~100 km wide Assam-Meghalaya Gneissic Complex (AMGC; Fig. 1b) represents an elevated Precambrian crustal block in northeastern India and is tectonically detached from the Indian peninsular shield by the Rajmahal-Garo tectonic graben (Eremenco et al., 1969). The Dauki fault bounds the AMGC to the south (Evans, 1964; Biswas and Grasemann, 2005), the Brahmaputra Valley fault to the north (Gupta and Sen, 1988; Bilham and England, 2001), the Jamuna fault to the west (Gupta and Sen, 1988) and the Naga Schuppen Belt (Indo-Myanmar mobile belt, IMMB) to the east. The easternmost extension of AMGC is represented by Mikir Hills, which is separated from the rest of the AMGC by the Kopili fault (Figs. 1b and 2a). The AMGC (including Mikir Hills) is characterized by metapelites (including gneissic variety), quartzo-feldspathic gneisses, mafic and calc-granulites, amphibolites and granitoids (Fig. 1b; Mazumdar, 1976; Nandy, 2001; Ghosh et al., 2005; Chatterjee et al., 2007; Yin et al., 2010). The gneisses are unconformably overlain by Shillong Group metasedimentary rocks (i.e., micaceous quartzite, phyllite, mudstone, sandstone, and quartz arenite) and Quaternary sediments (Nandy, 2001; Yin et al., 2010).

The metapelites in the western AMGC (e.g., Garo-Goalpara Hills) experienced prograde and peak *P–T* conditions of 4.5–5.0 kbar at 600–650 °C and 7.5 kbar at 850 °C, respectively. Monazite dating of these samples revealed the timing of this high-grade metamorphism at 1596 ± 15 Ma (Chatterjee et al., 2007, 2011). Similarly, the metapelites from Umpretha (central AMGC) and Sonapahar (central AMGC) regions recorded peak high-grade metamorphic conditions of 4.7–6.0 kbar at 710–760 °C (Chatterjee et al., 2011) and 5.8–8.2 kbar at 677–817 °C (Dwivedi et al., 2020), respectively. Chatterjee et al. (2011) constrained the timing of high-grade metamorphism in Umpretha metapelites at 494 ± 15 Ma, whereas Dwivedi et al. (2020) obtained the timing of peak metamorphism for Sonapahar metapelites at 478 ± 7 Ma. The AMGC is also composed of Mesoproterozoic granite gneisses (1400–1778 Ma; Bidyananda and Deomurari, 2007; Yin et al., 2010; Kumar et al., 2017) and Neoproterozoic intrusive granitoids (Kumar, 1990; Ghosh et al., 1991, 1994, 2005; Yin et al., 2010; Mazumdar and Dutta, 2016; Kumar et al., 2017). However, except for the geochemical and geochronological characteristics of granitoids, the *P–T–t* history of high-grade gneisses is poorly documented in the Mikir Hills region. The present study deciphers the metamorphic history of gneisses exposed in the Mikir Hills region to understand the tectonothermal evolution of the easternmost segment of the AMGC (Fig. 2a–c).

3. Field relations and sample descriptions

The migmatised pelitic and quartzo-feldspathic gneisses of the Mikir Hills region occur as inliers within the Shillong Group of metasedimentary rocks and Quaternary sediments (Fig. 2a-c). Mesoscopically, the abundance of mica minerals, garnet, and cordierite are helpful in distinguishing pelitic and quartzo-feldspathic gneisses (Fig. 3a–i). The pelitic gneisses are well exposed near the Lang Phocheng area and associated with quartzo-feldspathic gneisses and foliated granitoids (Figs. 2a–b and 3a–e). The gneisses are characterized by a dominant ENE–WSW striking and shallow- to moderately-dipping (< 40°) gneissic foliation S_2 (Figs. 2b and 3a, d). Locally, the gneissic foliation shows small-scale shallow-plunging (< 15° towards NNW) upright folds with weakly developed S_3 axial planar fabric (Fig. 3d). The orientation of penetrative fabric in foliated granites (Fig. 3e) is similar to that observed in gneisses, and evolves into a steeply-dipping (up to 70°) gneissic foliation near Mahamaya Parbat area (Fig. 2b). The early S_1 foliation, occurring as interfolial folds within S_2 gneissosity of quartzo-feldspathic gneisses, is preserved as tight to isoclinal folds in northeastern parts (Moha Kro and Sarbura Terang areas) of the Mikir Hills (Fig. 3f, g). These areas are dominated by steeply-dipping (up to 80°) S_3 axial planar foliation (Fig. 3h), which developed due to the shallow-plunging upright folds on S_2 gneissosity (Figs. 2c and 3i).

The pelitic gneisses collected from the Lang Phocheng area are defined by centimetre-scale alternate leucocratic (K-feldspar > plagioclase > garnet > quartz > sillimanite) and melanocratic (plagioclase > biotite > K-feldspar > quartz) layers (samples G52 and G53; Figs. 2b and 3a–d; Table 1). The non-garnetiferous quartzo-feldspathic gneisses (K-feldspar > plagioclase > quartz > biotite > opaques) are well preserved in and around Lang Phocheng, Kakoti Kro, and Ganeshpur areas (Figs. 2b and 3d; Table 1). However, the garnet-bearing migmatised quartzo-feldspathic gneisses (G54 and G55) are best exposed in the northeastern parts of Mikir Hills around Sarbura Terang and Moha Kro areas (Figs. 2c and 3f–i). Mesoscopically, these gneisses are classified as schlieren diatexites (cf. Ashworth and McLellan, 1985; Sawyer, 1998; Milord et al., 2001) and show alternate leucocratic (K-feldspar >> plagioclase > quartz > biotite > garnet) and melanocratic layers (biotite >> plagioclase > K-feldspar > quartz) layers (Fig. 3f).

4. Petrography and mineral chemistry

Two different types of gneisses, including migmatised pelitic gneisses and quartzo-feldspathic gneisses, are investigated from the Mikir Hills region. The petrographic characteristics, compositional variations and mineral paragenesis of representative pelitic (G52 and G53) and quartzo-feldspathic (G54 and G55) gneisses are presented in Figs. 4 – 8. Detailed mineral compositions of these samples are given in Supplementary Data Table S1. Mineral abbreviations are followed after Whitney and Evans (2010).

4.1. Sample G52 (pelitic gneiss)

Sample G52 shows a gneissic structure with alternate leucocratic and melanocratic layers and is composed (vol.%) of garnet porphyroblasts (~14%), matrix minerals such as quartz (~32%), plagioclase (~18%), K-feldspar (~16%), cordierite (~8%), biotite (~6%) and sillimanite (~5%) with ilmenite, rutile, spinel, zircon and monazite as accessory minerals (Fig. 4a; Tables 1 and 2). The prograde (M_{PR}) and peak (M_P) metamorphic assemblages in this sample are represented by $Bt_1 + Qz + Ilm + Rt \pm Pl_1 \pm Sil_1$ and $Grt_{core} + Kfs + Sil_1 + Bt_2 + Pl_2 + Qz + Ilm \pm Rt$, respectively. The post-peak (M_{PP}) metamorphic episode is indicated by $Grt_{rim} + Crd + Spl + Kfs + Sil_2 + Bt_{2rim} + Pl_3 + Qz + Ilm$ assemblage.

The early foliation (S_1), developed due to D_1 deformation, is represented by curved inclusion trails of quartz, biotite (Bt_1), plagioclase (Pl_1), ilmenite and rutile within garnet (Fig. 4a–c). Rutile is only observed as inclusion within garnet. The leucocratic (quartz > K-feldspar > sillimanite > plagioclase > garnet > biotite) and melanocratic (plagioclase > garnet > biotite > quartz > K-feldspar > sillimanite > ilmenite) layers define the pervasive S_2 foliation in the sample (Figs. 2b and 4a). The inclusion trails (S_1) in garnet are curved and show a low-angle relationship with external foliation (S_2), indicating that garnet porphyroblasts would have formed during the early stages of D_2 deformation (Figs. 4a, b and 8). Sillimanite occurs as lensoidal aggregates (Sil_1) that were wrapped by the S_2 foliation (Fig. 4a, e). The alignment of lensoidal sillimanite (Sil_1) along with the matrix biotite (Bt_2) defines the pervasive S_2 foliation in G52 (Fig. 4a–c). In addition to the inclusion-type plagioclase (Pl_1), two types of plagioclase grains, Pl_2 and Pl_3, are identified in the matrix. The anhedral plagioclase (Pl_1) inclusions typically form mantles around quartz inclusions in garnet, indicating the growth of Pl_1 during the initial stages of melt crystallization. The continued melting has resulted in the development of discrete plagioclase grains (Pl_2) in the melanocratic and leucocratic layers (Fig. 4a), whereas the narrow irregular films of plagioclase around the matrix minerals define Pl_3 grains (Fig. 4a, e). The K-feldspar-plagioclase (Pl_3) melt pseudomorphs surrounding lensoidal sillimanite (Sil_1) aggregates and quartz ribbons, and thin films of quartz and plagioclase (Pl_3) around garnet represent the melting signatures (Fig. 4a, d, e). These textural observations suggest that the partial melting in pelitic gneisses possibly occurred during D_2 deformation (Figs. 2b and 4a). Fine-grained elongated sillimanite (Sil_2) needles overgrow the S_2 foliation (Fig. 4d, f), indicating that Sil_2 growth post-dates D_2 deformation and possibly develop during D_3 deformation. Cordierite and quartz symplectites form along the embayed grain boundaries of garnet porphyroblasts and are preserved in the pressure shadow zones of garnets (Fig. 4g, h). Occasionally, cordierite is associated with spinel by developing symplectite texture (Fig. 4j), indicating the late-stage breakdown of garnet porphyroblasts. In addition, cordierite is also associated with matrix minerals of plagioclase (Pl_2), biotite (Bt_2) and sillimanite (Sil_1) (Fig. 4a). The elongated quartz ribbons with interlobate to polygonal grain boundaries suggest medium to high-temperature (Fig. 4f; ~500–700 ˚C; Passchier and Trouw, 2005) deformation for the pelitic gneisses.

Garnet is almandine-rich (X_{Alm} $[Fe^{+2}/(Fe^{+2}+Mg+Ca+Mn)] = 0.70–0.75$, X_{Prp} $[Mg/(Fe^{+2}+Mg+Ca+Mn)] = 0.20–0.23$, X_{Grs} $[Ca/(Fe^{+2}+Mg+Ca+Mn)] = 0.02–0.07$, X_{Sps} $[Mn/(Fe^{+2}+Mg+Ca+Mn)] = 0.01$), and compositional profiles show an increase in X_{Alm} content with relatively uniform concentrations of X_{Prp} and X_{Sps} from core to rim (Figs. 6a and 7a; Supplementary Data Table S1). Garnet shows significant zoning in X_{Grs} content with a decreased concentration from core ($X_{Grs} = 0.05–0.07$) to rim ($X_{Grs} = 0.02–0.05$) (Fig. 6a). The minimal amount of ferric ion content, calculated through the charge balance method, indicates the presence of insignificant andradite component in garnet (Supplementary Data Table S1). The

inclusion-rich garnet core represents a part of the peak metamorphic assemblage, whereas diffusional zoning recorded by garnet rims characterizes the post-peak metamorphic readjustments (cf. Spear and Florence, 1992; La Roche et al., 2015; Hrushikesh et al., 2019). Inclusion-type biotite (Bt_1) is Mg-rich (X_{Fe} = 0.36–0.43) and shows TiO_2 content in the range of 4.63–5.81 wt.%, whereas matrix biotite (Bt_2) is relatively Fe-rich (X_{Fe} [Fe/(Fe+Mg)] = 0.47 – 0.63) with similar TiO_2 (4.41–6.90 wt.%) concentration (Fig. 7c). The matrix biotite (Bt_{2rim}) associated with garnet has variable X_{Fe} values (0.42–0.45) and TiO_2 (3.51–4.02 wt.%) contents. The inclusion type plagioclase (Pl_1) has X_{Ab} [Na/(Na+Ca+K)] values of 0.46–0.59, whereas Pl_2 and Pl_3 in the matrix are characterized by X_{Ab} values of 0.65–0.71 and 0.73–0.77, respectively (Fig. 7b; Supplementary Data Table S1). Cordierite grains show uniform composition with X_{Fe} values of 0.36–0.41 and minor volatile components up to ~2 wt.%. Spinel grains show hercynite composition [X_{Hc} ($Fe^{2+} - 2\times Ti - 0.5\times(Fe^{3+} + Cr)$) = 0.67 – 0.75] with Al_2O_3 and ZnO values of 57.42–59.15 wt.% and 2.60–5.62 wt.%, respectively. Ilmenite grains occurring as inclusions within garnet and those in the matrix show similar composition with uniform X_{Fe} (0.96–0.97) values (Supplementary Data Table S1).

4.2. Sample G53 (pelitic gneiss)

Structurally, pelitic gneiss samples (G53 and G52) show dominant S_2 foliation but show variation in mineral abundances. This sample is composed (vol.%) of garnet (~5%), matrix quartz (~46%), cordierite (~16%), K-feldspar (~9%), plagioclase (~7%), biotite (~4%) and sillimanite (~4%) with accessory ilmenite, rutile, zircon and monazite (Fig. 4j; Tables 1 and 2). The prograde (M_{PR}) and peak (M_P) metamorphic assemblages in this sample are represented by Bt_1 + Qz + Ilm + Rt ± Kfs ± Sil_1 ± Pl_1 and Grt_{core} + Kfs + Sil_1 + Bt_2 + Pl_2 + Qz + Ilm ± Rt, respectively. The post-peak (M_{PP}) metamorphic episode is represented by Grt_{rim} + Crd + Kfs + Sil_2 + Bt_{2rim} + Qz + Ilm assemblage.

Garnet porphyroblasts are inclusion-poor and rarely contain inclusions of quartz, plagioclase (Pl_1), biotite (Bt_1), ilmenite and rutile (Fig. 4k–m). Although garnet lacks internal foliation, the absence of pressure shadow zones around garnet indicates syn-to post-kinematic growth of garnet with respect to S_2 matrix foliation (Fig. 4k–m). The alignment of matrix biotite (Bt_2) and sillimanite aggregates (Sil_1) defines the schistosity in this sample. Breakdown of the garnet has resulted in cordierite and sillimanite (Sil_2) formation along the garnet grain boundaries (Fig. 4k, l). Plagioclase in the matrix occurs as discrete grains in melanocratic and leucocratic layers (Pl_2) and also forms thin films (Pl_3) in the matrix that develop as a product of melt crystallization. The discrete plagioclase grains formed in the melanocratic and leucocratic layers represent Pl_2 grains (Fig. 4l, m), whereas the thin films of plagioclase around the matrix minerals characterize Pl_3 grains (Fig. 4k). Cordierite also occurs as a discrete mineral, indicating that cordierite would have formed due to the breakdown of matrix biotite (Bt_2) and sillimanite (Sil_1). The bulging and grain boundary migration microstructures (Fig. 4l) indicate dynamic recrystallization of quartz at elevated temperature conditions (> 600 ˚C; Passchier and Trouw, 2005).

Garnet porphyroblasts are almandine-rich (X_{Alm} = 0.83–0.85, X_{Prp} = 0.09–0.11, X_{Grs} = 0.02–0.04, X_{Sps} = 0.01). The compositional profile shows an increase in X_{Alm} content and a decrease in X_{Prp} and X_{Grs} contents from core to rim (Fig. 6b). X_{Sps} content in garnet is homogenous from core to rim. Inclusion-type biotite (Bt_1) is Fe-rich (X_{Fe} = 0.64–0.66) and shows TiO_2 content in the range of 3.51–5.36 wt.%. The matrix biotite (Bt_2) is relatively enriched in Fe content (X_{Fe} = 0.67 – 0.74) with slightly lower TiO_2 (3.02–4.45 wt.%) concentration (Fig. 7c; Supplementary Data Table S1). The matrix biotite (Bt_{2rim}) in contact with garnet shows X_{Fe} values 0.58–0.60 with and TiO_2 contents of 2.85–3.13 wt.% (Fig. 7c; Supplementary Data Table S1). The inclusion-type plagioclase grains (Pl_1) show X_{Ab} values of 0.51–0.68. On the other hand, matrix (Pl_2) type plagioclase and thin films of plagioclase (Pl_3) are characterized by X_{Ab} values of 0.73–0.76 and 0.73–0.77, respectively (Fig. 7b). Cordierite grains show mostly uniform X_{Fe} values of 0.54–0.57 with volatile components up to 2 wt.%. The inclusion-type and matrix-type ilmenite grains show similar composition with X_{Fe} values of 0.96–0.97.

4.3. Sample G55 (quartzo-feldspathic gneiss)

The sample G55 is characterized by well-developed gneissosity, showing alternate leucocratic and melanocratic layers (Fig. 2b). The leucocratic layer of the gneiss is composed of plagioclase (~43 vol.%), quartz (~40 vol.%), K-feldspar (~11 vol.%), biotite (~3 vol.%), ilmenite (~1 vol.%) and garnet (< 1 vol.%) (Fig. 5a; Tables 1 and 2). The melanocratic layer consists of biotite, plagioclase, K-feldspar, quartz and ilmenite. The peak mineral assemblage in this sample is represented by garnet + plagioclase + K-feldspar + biotite + quartz + ilmenite + melt assemblage. Garnet porphyroblasts are inclusion-free and developed in the leucocratic layers (Fig. 5a). The garnet porphyroblasts are spessartine-rich (X_{Alm} = 0.36–0.39, X_{Prp} = 0.04–0.07, X_{Grs} = 0.02–0.03, X_{Sps} = 0.53–0.55) and show uniform composition from core to rim (Figs. 6c and 7a). A weak diffusional zoning is observed in X_{Prp} concentration at the garnet rim (Fig. 6c). Biotite forms as a matrix mineral with X_{Fe} and TiO_2 concentrations of 0.51–0.52 and 2.11–2.60 wt.%, respectively. The matrix biotite shows slightly different composition (X_{Fe} = 0.53; TiO_2 = 1.80–1.82 wt.%) at the garnet grain boundaries (Fig. 7c). The composition of matrix plagioclase shows X_{Ab} values of 0.84 and 0.86 (Fig. 7b; Supplementary Data Table S1). Ilmenite grains are enriched in Mn content (0.04–0.30 pfu) with exsolution of titanomagnetite (X_{Fe2+} = 0.88 – 0.98).

4.4. Sample G54 (quartzo-feldspathic gneiss)

This sample represents the leucocratic part of the quartzo-feldspathic gneiss and is composed of quartz (~35%), plagioclase (~32%), K-feldspar (~24%), biotite (~3%), magnetite (< 2 vol.%), garnet (< 1%) and chlorite (< 1%) with accessory muscovite, ilmenite and monazite (Fig. 5b; Tables 1 and 2). The melanocratic layer comprises biotite, plagioclase, K-feldspar, quartz and ilmenite. The peak mineral assemblage in this sample is represented by garnet +

plagioclase + K-feldspar + biotite + quartz + ilmenite + melt assemblage. Garnet formed post-kinematic with matrix minerals and is chemically homogeneous with enriched almandine and spessartine contents (X_{Alm} = 0.51–0.54, X_{Prp} = 0.03–0.04, X_{Grs} = 0.03–0.05, X_{Sps} = 0.40–0.41) (Fig. 5c; Supplementary Data Table S1). Plagioclase grains show X_{Ab} values of 0.80 – 0.91 (Fig. 7a, b). The matrix biotite is characterized by X_{Fe} and TiO_2 concentrations of 0.71–0.72 and 1.99–3.22 wt.%, respectively (Fig. 7c). Ilmenite grains show enriched Mn content (0.12–0.29 pfu). Rarely occurring muscovite grains show homogeneous composition with Si values of 3.13–3.20 pfu, and chlorite in the matrix shows enriched X_{Fe} content of 0.70–0.71.

5. Mineral paragenesis

5.1. Prograde (M_{PR}) and Peak metamorphism (M_P) in pelitic gneisses

In pelitic gneisses (G52 and 53), biotite (Bt_1) + rutile + ilmenite + quartz ± plagioclase (Pl_1) ± sillimanite (Sil_1) minerals represent the prograde assemblage (M_{PR}). The occurrence of lensoidal sillimanite (Sil_1) aggregates, K-feldspar, and quartz in the matrix indicates that the rock experienced melting under second sillimanite isograd conditions (Fig. 4). The sample lacks muscovite grains, possibly suggesting that muscovite would have been completely consumed during prograde melting. This prograde metamorphism would have stabilized matrix biotite (Bt_2), and its subsequent melting developed plagioclase (Pl_2) and K-feldspar. Garnet appears to have formed during the late stage of melting by engulfing the minerals in leucocratic layers. Therefore, garnet core + K-feldspar + sillimanite (Sil_1) + biotite (Bt_2) + plagioclase (Pl_2) + quartz + ilmenite assemblage (M_P) defines the peak metamorphic episode in pelitic gneisses (Fig. 8). The formation of peak metamorphic assemblage can be explained by the following KFMASH dehydration melting reaction (Pickering and Johnston, 1998):

$$Bt_1 + Pl_e + Sil_1 + Qz = Grt + Pl_1 + Kfs + Liq \quad (1)$$

The above-melting reaction forms plagioclase (Pl_1) by recrystallizing the pre-existing plagioclase (Pl_e) in the protolith. As a result, the Pl_1 is enriched in calcium component because the sodium component of Pl_e would typically be portioned into melt (cf. Vernon and Clarke, 2008). The continued melting has resulted in the growth of relatively sodium-rich plagioclase (Pl_2). This inference is consistent with an increase in the sodic component of Pl_2 (X_{Ab} = 0.65–0.73) relative to Pl_1 (X_{Ab} = 0.46–0.68). Eventually, the plagioclase (Pl_3) crystallized from the final stage of melt is enriched in the sodic component, which corroborates the growth of thin films of sodic plagioclase (Pl_3; X_{Ab} = 0.73–0.77) in the leucocratic and melanocratic layers (Figs. 4a, e, k and 7b).

5.2. Post-peak metamorphism (M_{PP}) in pelitic gneisses

During post-peak metamorphism, garnet breakdown produced cordierite-quartz and cordierite-spinel symplectites along its grain boundaries. This has resulted in the Fe-Mg compositional zoning along the garnet rims (Fig. 4g–i). The formation of cordierite and cordierite–spinel assemblages can be explained by the following FMAS reactions (Hensen, 1971; Clarke and Powell, 1991):

$$Grt + Sil_1 = Crd + Spl \quad (2)$$

$$Grt + Sil_1 + Qtz = Crd + Spl \quad (3)$$

The cordierite is also observed as a breakdown product of matrix minerals, such as biotite (Bt_2) and sillimanite (Sil_1) (Fig. 4a, j and k). The following KFMASH reaction explains the stability of cordierite from matrix minerals (Hoffer, 1976):

$$Bt_2 + Sil_1 + Qz = Crd + Kfs + H_2O \quad (4)$$

The growth of fine-grained sillimanite (Sil_2) around garnet porphyroblasts indicates garnet breakdown during retrograde metamorphism (Fig. 4f). During this metamorphism, matrix biotite shows compositional readjustments along the garnet grain boundaries. The following KFMASH reaction explains the stability of retrograde minerals (Mahan et al., 2006):

$$Grt + Kfs + H_2O = Bt_{2rim} + Sil_2 + Qz \quad (5)$$

5.3. Peak metamorphism in quartzo-feldspathic gneisses

The migmatised quartzo-feldspathic gneisses (G54 and G55) are characterized by the stability of idioblastic garnet, overgrowing the matrix minerals composed of plagioclase–K-feldspar–biotite–quartz in the leucocratic layer (Fig. 5). Field and textural observations suggest that these gneisses have undergone significant melting. The stability of garnet and melt in quartzo-feldspathic gneisses can be related by the following KFMASH melting reaction (Braun et al., 1996):

$$Bt + Pl + Qz = Grt + Kfs + Liq \quad (6)$$

The above-mentioned metamorphic reactions infer that the mineral assemblages in migmatised pelitic and quartzo-feldspathic gneisses experienced metamorphism under upper amphibolite to granulite facies conditions.

6. Estimation of pressure–temperature conditions

6.1. Conventional thermobarometry

The peak and post-peak metamorphic conditions of migmatised pelitic gneisses (G52 and G53) and quartzo-feldspathic gneisses (G55) were estimated using the mineral assemblages identified for different metamorphic episodes (Fig. 8). The results of conventional thermobarometry are summarized in Table 3. The temperature conditions were estimated using the garnet-biotite (Ganguly et al., 1996; Holdaway, 2000), garnet-cordierite (Bhattacharya et al., 1988), spinel-cordierite (Vielzeuf, 1983) and Ti-in-biotite (Henry et al., 2005) thermometers. The pressure conditions were calculated using the garnet-biotite-plagioclase-quartz (GBPQ; Wu et al., 2004), garnet-aluminum silicate-quartz-plagioclase (GASP; Ganguly et al., 1996), garnet-biotite-aluminum silicate-quartz (GBAQ; Wu et al., 2017) and garnet-cordierite-sillimanite-quartz (GCSQ; Perchuk et al., 1985) barometers. The calculated pressure and temperature conditions using conventional thermobarometry are typically associated with ±1 kbar and ±50 °C errors, respectively (Table 3). These errors resulted from the uncertainties associated with the thermodynamic dataset of solid solution phases, activity-composition relationships of mineral phases, and analytical error propagated with the estimation of mineral compositions (Powell and Holland, 2008; Palin et al., 2016; Deshmukh et al., 2017).

6.1.1. Peak metamorphic (M_P) conditions for pelitic gneisses

The mineral compositions of garnet core, matrix biotite (Bt_2) and plagioclase (Pl_2) were used for calculating peak metamorphic conditions. The thermometers using garnet (core)–matrix biotite (Bt_2) pairs (Ganguly et al., 1996; Holdaway, 2000) and garnet (core)-biotite (Bt_2)-plagioclase (Pl_2)-quartz (GBPQ; Wu et al., 2004) assemblage yielded peak (M_P) *P–T* conditions of 7.5–8.4 kbar at 674–778 °C and 5.7–7.4 kbar at 620–767 °C for samples G52 and G53, respectively. The Ti-in-biotite thermometry gives similar temperature conditions for samples G52 (740–777 °C) and G53 (645–728 °C). The application of garnet (core)-sillimanite (Sil_1)-quartz-plagioclase (Pl_2) (GASP; Ganguly et al., 1996) and garnet (core)-biotite (Bt_2)-aluminosilicate (Sil_1)-quartz (GBAQ; Wu et al., 2017) barometers yields relatively lower pressure ranges for G52 (4.79–6.59 kbar) and G53 (4.23–6.43 kbar) than GBPQ barometer.

6.1.2. Post-peak metamorphic (M_{PP}) conditions for pelitic gneisses

The post-peak metamorphic conditions were estimated using the compositions of matrix minerals [i.e., biotite (Bt_{2rim}) and cordierite] that are in contact with the garnet rim. The garnet rim–biotite (Bt_{2rim}) pairs (Ganguly et al., 1996; Holdaway, 2000) and garnet (rim)–biotite (Bt_{2rim})–aluminosilicate (Sil_2)–quartz (GBAQ; Wu et al., 2017) mineral assemblage yielded post-peak (M_{PP}) *P–T* conditions of 2.14–2.52 kbar at 563–660 °C for sample G52 and 2.45–2.71 kbar at 495–583 °C for sample G53. However, garnet (rim)-cordierite pairs yielded post-peak temperature conditions at 670–708 °C and 564–599 °C for samples G52 and G53, respectively. In contrast, the application of Ti-in-biotite thermometry yielded much higher temperature conditions for the matrix biotite (Bt_{2rim}) grains in contact with garnet (G52 = 715–759 °C; G53 =

645–676 °C; Table 3). These temperatures are slightly higher than those obtained using garnet-biotite and garnet-cordierite pairs due to the higher blocking temperatures for Ti in biotite relative to Fe-Mg exchange (Henry et al., 2005). In addition, the application of garnet (rim)–cordierite–sillimanite (Sil_2)–quartz (GCSQ) barometer gives pressure ranges of 4.1–4.4 kbar (G52) and 2.34–2.75 kbar (G53).

6.1.3. Peak metamorphic conditions for quartzo-feldspathic gneisses

Garnet porphyroblast shows uniform composition in the quartzo-feldspathic gneiss (sample G55). The mineral pairs of garnet-biotite (Holdaway, 2000) and GBPQ (Wu et al., 2004) assemblage yielded peak *P–T* conditions of 6.7–7.4 kbar and 601–618 °C. The application of Ti-in-biotite (Henry et al., 2005) thermometry yielded similar temperature conditions of 625–658 °C (Table 3). However, the garnet-biotite thermometer by Ganguly et al. (1996) yielded lower temperatures (496–531 °C) than the values of Holdaway (2000). The Ganguly et al. (1996) thermobarometer uses thermobarometric data for Fe-Mg-Ca-Mn garnets and assumed ideality for the co-existing biotite. This assumption would have led to some uncertainty on the pressure and temperature estimates of Ganguly et al. (1996).

6.2. Phase equilibrium modelling and metamorphic P–T path

P–T pseudosection modelling was carried out using the Perple_X software program (version 6.9.1; Connolly, 2005), which uses an internally consistent thermodynamic data set (hp62ver.dat) after Holland and Powell (1998) and updated in 2011. Pseudosection modelling was performed in the MnNCKFMASHTO system (MnO-Na_2O-CaO-K_2O-FeO-MgO-Al_2O_3-SiO_2-H_2O-TiO_2-O_2), which provides realistic phase equilibria representation for the pelitic to quartzo-feldspathic rocks (cf. Endo et al., 2012; White et al., 2014). The activity–composition (a–x) solution models in the study of pelitic and quartzo-feldspathic gneisses are garnet, biotite, white mica, cordierite, orthopyroxene, and silicic melt (White et al., 2014), K-feldspar (Waldbaum and Thompson, 1968), plagioclase (Newton et al., 1980) and spinel (White et al., 2002). The whole rock compositions usually represent the residual bulk composition after melt loss and are suitable for determining the peak and post-peak metamorphic conditions of migmatised rocks (White et al., 2004). The bulk compositions for the studied samples were estimated by combining the mineral mode proportions obtained using the XMapTools program (Lanari et al., 2014). This method uses ten-element X-ray element maps obtained for the entire thin section while computing the modal abundance of minerals present in the rock (Figs. 4a, j and 5a, b). This approach precisely estimates the modal proportions of hydrous minerals and Fe^{+3}-bearing minerals (biotite, spinel and garnet) in the rock, which are used to calculate the bulk H_2O and O_2 contents of the samples. The possible source of errors in the estimation of bulk composition include uncertainties from (a) the selection of representative areas for mineral mode calculations (Palin et al., 2016) and (b) the cumulative error associated with mode calculations of major and fine-grained minerals using XMapTools program (Lanari et al., 2014). However, these

uncertainties have a negligible effect on the overall bulk composition of the rock (Lanari et al., 2014; Palin et al., 2016).

The prograde metamorphic evolution of migmatised samples can be evaluated by estimating the possible protolith composition, and this involves the reintegration of melt that was lost from the system into the residual bulk composition (White et al., 2004; Diener et al., 2008). The melt accumulated in the rock begins to escape from the system when it reaches 7 vol.% and is generally regarded as the upper limit for melt drain (Rosenberg and Handy, 2005). However, approximately 1 vol.% of the melt can be retained along the grain boundaries (Sawyer, 2001), indicating an overall melt loss of 6 vol.% for a single prograde melting event. In this study, we used the down-temperature melt reintegration method (Korhonen et al., 2013), which adds the lost melt to the residual composition to retrieve the possible protolith bulk compositions for the migmatised gneisses. The *P–T* pseudosections constructed for the studied samples are shown in Figs. 9, 10 and Supplementary Data Fig. S1. The normalized bulk compositions used for pseudosection modelling are summarized in Table 4.

6.2.1. Migmatised pelitic gneisses (G52 and 53)

The *P–T* pseudosections for pelitic gneisses are constructed in a *P–T* range of 2–12 kbar and 500–900 °C (Fig. 9a–d). Petrographically, both these samples contain similar peak (M_P: garnet (core) + biotite (Bt_2) + sillimanite (Sil_1) + K-feldspar + plagioclase (Pl_2) + quartz + ilmenite + melt) and post-peak (M_{PP}: garnet (rim) + cordierite + biotite (Bt_{2rim}) + sillimanite (Sil_2) + K-feldspar + plagioclase (Pl_3) + quartz + ilmenite ± spinel) metamorphic assemblages.

In sample G52, the peak metamorphic assemblage is stable over a *P–T* range of 5.0–8.5 kbar and 770–800 °C (Fig. 9a). The intersection of garnet core (X_{Alm} = 0.70–0.71, X_{Prp} = 0.21–0.23 and X_{Grs} = 0.05–0.06), biotite (Bt_2; X_{Fe} = 0.46–0.51) and plagioclase (Pl_2; X_{Ab} = 0.69–0.71) isopleths is used to constrain the peak metamorphic conditions at 8.0–8.6 kbar and 768–780 °C. The post-peak metamorphic conditions (M_{PP}) are estimated using the garnet rim (X_{Fe} = 0.73–0.74, X_{Mg} = 0.21–0.22 and X_{Ca} = 0.03–0.04) and cordierite compositions (X_{Fe} = 0.36–0.39) at 4.0–5.0 kbar and 720–765 °C (Fig. 9a). Although spinel is stable in the post-peak assemblage, the estimated *P–T* conditions fall within the spinel-absent stability field. This is because pseudosection modelling is unsuitable for modelling mineral phases in such a small volume. Based on petrographic characteristics, spinel accounts for < 0.1 vol.% of the rock and therefore not stable at the calculated *P–T* conditions. Furthermore, the spinel–magnetite solution model employed in the pseudosection modelling does not account for the effect of Mn, Cr and Zn in the solid solution (White et al., 2002). Therefore, the presence of significant amount of gahnite component (ZnO = 2.6 – 5.5 wt.%) in spinel suggests possible deviation in the stability field of spinel (> 800 °C and 4 kbar; Fig. 9a). Similarly, plagioclase (Pl_3) isopleths were ignored while estimating post-peak metamorphic conditions in the phase diagram. Based on compositional difference, it is evident that Pl_3 plagioclase is more evolved (rich in X_{Ab}) than those formed during the early stages of migmatisation (rich in X_{An}; Pl_1 and Pl_2), indicating a change in the effective bulk composition from peak to post-peak metamorphism. However, the change of effective bulk composition is not accounted while performing the pseudosection modelling. The estimated peak and post-peak metamorphic conditions (M_P–M_{PP}) suggest a near-isothermal

decompression path (Fig. 9a). For estimating prograde metamorphic conditions, approximately 6 vol.% of melt was added to the residual bulk composition, representing the first stage of melt reintegration. The reintegrated bulk composition was used to compute a separate pseudosection (Fig. 9d and Supplementary Data Fig. S1). The procedure is repeated for the second and third stages of melt reintegration by adding 12 vol.% and 18 vol.% of melt to the system, respectively. The corresponding pseudosections constrain the H_2O saturated prograde assemblage (M_{PR}: biotite + plagioclase + quartz + rutile ± garnet ± sillimanite ± muscovite) in a range of 5.5–7.5 kbar and 645–695 °C (Fig. 9b). The absence of muscovite in the sample indicates that the muscovite would have consumed entirely during the prograde melting process. The combination of M_{PR}–M_P and M_P–M_{PP} conditions suggests a clockwise *P–T* path involving prograde heating and isothermal decompression (Fig. 9b).

For sample G53, the pseudosection topology is similar to sample G52. The peak metamorphic assemblage is stable in a *P–T* range of 3.5–8.0 kbar and 720–770 °C (Fig. 9c). The intersection of garnet (X_{Alm} = 0.83–0.84, X_{Prp} = 0.10–0.11 and X_{Grs} = 0.03–0.04), biotite (Bt_2; X_{Fe} = 0.68–0.74) and plagioclase (Pl_2; X_{Ab} = 0.72–0.74) isopleths constrain the peak metamorphic conditions at 5.8–7.5 kbar and 715–750 °C (Fig. 9c). The post-peak melt crystallization is marked by the growth of cordierite along the subhedral margins of garnet and compositional readjustments in garnet rim. The intersection of garnet rim composition (X_{Fe} = 0.85–0.86, X_{Mg} = 0.09–0.10 and X_{Ca} = 0.02) and cordierite composition (X_{Fe} = 0.56–0.57) yielded post-peak metamorphism conditions at 2.0–3.8 kbar and 640–730 °C (Fig. 9c). For characterizing prograde stage, the melt reintegration is carried out in the field of peak metamorphic assemblage at 7.25 kbar and 720 °C (Fig. 9d). Approximately 6 vol.% of melt was added to the residual bulk composition, representing the first stage of melt reintegration. The reintegrated new bulk composition was used to compute a new pseudosection (Fig. 9d and Supplementary Data Fig. S1). The second stage of melt reintegration is performed by adding 12 vol.% of melt to the system, and prepared the corresponding pseudosection using the new bulk composition (Fig. 9d and Supplementary Data Fig. S1). These results constrain the equilibrium conditions of H_2O saturated prograde assemblage (M_{PR} = K-feldspar + plagioclase + biotite + quartz + rutile ± ilmenite ± muscovite) up to 10 kbar and 625 °C. The combination of M_{PR}–M_P and M_P–M_{PP} conditions suggests a clockwise *P–T* path for the sample, involving prograde heating and isothermal decompression (Fig. 9d).

6.2.2. Migmatised quartzo-feldspathic gneiss (G55)

The pseudosection for sample G55 is constructed in the MnNCKFAMSHTO system using the residual bulk composition in a *P–T* range of 2–12 kbar and 500–900 °C (Fig. 10). The observed metamorphic assemblage (garnet + K-feldspar + plagioclase + biotite + ilmenite + quartz + melt) is stable over a wide *P–T* range of 3.0 to > 12.0 kbar and 600–820 °C (Fig. 10). However, the compositional isopleths of Mn-rich garnet (X_{Alm} = 0.36–0.38, X_{Prp} = 0.05–0.08 and X_{Grs} = 0.02–0.03), biotite (X_{Fe} = 0.52–0.53) and plagioclase (X_{Ab} = 0.84–0.86) intersects at much lower *P–T* conditions of 3.8–4.6 kbar and 590–650 °C (Fig. 10). Further, the absence of melt at these *P–T* conditions suggests that the garnet crystallized below the solidus. This inference is consistent with the growth of subhedral garnet showing uniform composition. The estimated *P–T* conditions indicate that the peak metamorphism and partial

melting occurred at much higher temperatures. Therefore, the possible *P–T* conditions in melt bearing and melt-absent fields define an approximate cooling *P–T* history for the quartzo-feldspathic gneiss (Fig. 10).

7. Geochronology

7.1. In situ U–Pb zircon dating

U–Pb zircon dating was performed for pelitic (G53) and quartzo-feldspathic (G55) gneisses using the GeOHeLiS platform facilities at the University of Rennes, France. Back-scattered (BSE) and cathodoluminescence (CL) imaging were performed on two polished thin sections to identify zircon grains and document the internal zoning patterns. The details of analytical settings are described in Supplementary Data Text, and the analytical conditions are tabulated in Supplementary Data Table S2. All uncertainties are reported at the 2σ level, and systematic uncertainties are propagated to the final dates following Horstwood et al. (2016). The systematic uncertainty, which is applied to the age of the population, is indicated in italics within brackets for the concordant dates. The Concordia diagrams were constructed using the IsoplotR software (Vermeesch, 2018). The CL zoning patterns and U–Pb zircon data are presented in Fig. 11 and Table 5 and Supplementary Data Table S3. Analytical data obtained for unknowns and GJ-1 zircon standard (used as quality control material) are given in Supplementary Data Table S3.

Zircon grains in the migmatised pelitic gneiss (G53) are subhedral to euhedral with lengths of 40 to 100 μm. Based on morphology, two zones are identified in zircon grains. These include inclusion-bearing cores and inclusion-poor overgrowths (Fig. 11a, b). Zircon cores contain rare inclusions of apatite and silicate minerals, whereas overgrowths on cores are characterized by periodic oscillatory zoning. These grains show oscillatory to patchy zoning and are characterized by bright-CL cores and dark-CL rims (Fig. 11a). As the dark-CL rims are too narrow (< 20 μm) for spot analysis, bright-CL cores were selected for U–Pb dating. Three of the analyses yield a concordant date of 1647 ± 11 (±*16*) Ma (MSWD = 1.3; Fig. 11a). Thirteen analyses define a Discordia with an upper intercept of 1683 ± 44 (±*45*) Ma (MSWD = 1.4; Fig. 11a). The bright-CL cores of zircon grains show oscillatory growth zoning with variable Th/U ratios (0.59–1.01; Table 5), indicating magmatic origin for these grains (Williams and Claesson, 1987; Hoskin and Black, 2000; Rubatto, 2002). Morphology, internal zoning patterns, and chemical compositions suggest that the zircon grains crystallized during the early to late magmatic stage. Therefore, the concordant date obtained from the zircon core (1647 ± 11 Ma) and upper intercept age of 1683 ± 44 Ma are interpreted as the crystallization age of an igneous protolith.

Zircon grains from the migmatised quartzo-feldspathic gneiss (G55) are subhedral to euhedral prismatic grains with a long axis of grains variable between 40 and 80 μm (Fig. 11b). These grains show weakly zoned dark-CL xenocrystic cores surrounded by intermediate CL

zones with oscillatory zoning, and bright-CL recrystallized rims. Occasionally, the cores of zircon grains contain inclusions of apatite and silicate minerals, whereas overgrowth zones lack mineral inclusions. The xenocrystic cores and recrystallized rims are too narrow for analysis, so the oscillatory zones were considered for U–Pb dating. Six analyses from five zircon grains yielded a concordant date of 1590 ± 7 (±*14*) Ma (MSWD = 1.0; Fig. 11b). Sixteen analyses define a Discordia with an upper intercept of 1613 ± 19 (±*22* Ma (MSWD = 1.3; Fig. 11b). The Th/U ratios from oscillatory zones are variable between 0.31 and 1.82 (Table 5), suggesting an igneous origin for these grains. Zircon internal structures, compositional variations and overlapping of core and overgrowth U–Pb ages indicate that zircon grains were formed during early to late magmatic stages (cf. Wang et al., 2014; Jiang et al., 2019). Therefore, we interpret the Concordia (1590 ± 7.3 Ma) and Discordia upper intercept (1613 ± 19 Ma) dates as the crystallization age of an igneous protolith.

7.2. U–Th–total Pb monazite dating

Monazite dating was performed on migmatised pelitic gneisses (G52 and G53) and quartzo-feldspathic gneisses (G54 and G55) from the Mikir Hills region. X-ray element mapping (YL_a, ThM_a, UM_b and PbM_a) of monazite grains has been performed to identify different chemical zones. According to Williams et al. (2006), the weighted mean of U-Th-total Pb dates obtained from a single chemical domain can represent the timing for a specific geological event. Therefore, the simultaneous processing of these X-ray maps (cf. Williams et al., 2006) is helpful in identifying two distinct compositional domains in pelitic (CD_P1 and CD_P2) and quartzo-feldspathic gneisses (CD_Q1 and CD_Q2) (Fig. 12). In addition, the monazite spot ages were processed using CHIME (chemical Th-U-total Pb isochron method) dating approach (Suzuki et al., 1991; Suzuki and Kato, 2008), which is useful to determine meaningful data from a homogeneous age domain showing notable chemical variation. The combination of these two approaches is helpful in identifying mixed ages in the multiple monazite spot ages (Fig. 12 and Supplementary Data Fig. S2; Table 5 and Supplementary Data Table S4).

Subhedral to anhedral monazite grains in sample G53 occur as inclusions in matrix minerals composed of quartz, K-feldspar and plagioclase. A few grains are hosted within the biotite grains that define the pervasive foliation. X-ray element maps of Th and Y show two distinct compositional domains, CD_P1 and CD_P2 (Fig. 12a, b). The compositional domain CD_P1 represents patchy zones in monazite and composed on low-Y and low-Th/U contents (Y_2O_3 = 0.37–1.84 wt.%; ThO_2 = 3.90–4.95 wt.%; UO_2 = 0.24–1.08 wt.%). The zones around CD_P1 represent the domain CD_P2 and composed of moderate-Y and high-Th/U contents (Y_2O_3 = 0.30–2.81 wt.%; ThO_2 = 4.20–5.48 wt.%; UO_2 = 0.17–0.36 wt.%; Table 5 and Supplementary Data Table S4). Spot analysis on CD_P1 and CD_P2 domains yielded age populations of 1058 ± 35 Ma (n = 6; MSWD = 1.8) and 467 ± 16 Ma (n = 5; MSWD = 0.24), respectively (Fig. 12c).

The monazite grains in sample G52 occur in various sizes (~50 μm–600 μm) and are hosted as inclusions within garnet porphyroblasts and quartzo-feldspathic matrix in the leucocratic layers (Fig. 12d, e). These monazite grains show sector and oscillatory growth zones

and are characterized by low Y content with variable concentrations of Th and U (Y_2O_3 = up to 0.59 wt.%, ThO_2 = 5.21–10.76 wt.%, UO_2 = 0.11–1.62 wt.%; Table 4 and Supplementary Data Table S4). The zoning identified in this sample is equivalent to the CD_P2 domain of sample G53. Despite showing compositional zoning, monazite grains yielded a single-age population of 480 ± 8 Ma (n = 31; MSWD = 2.8) (Fig. 12f).

Monazite grains in sample G54 are hosted in the quartzo-feldspathic matrix, displaying concentric growth zoning (CD_Q1) and sporadic patchy zoning (CD_Q2). X-ray element maps show wide variation in Y, Th and U contents of monazite grains (Fig. 12g, h). The CD_Q1 is characterized by low LREE and high Th/U contents (Y_2O_3 = 1.69–2.90 wt.%; ThO_2 = 8.71–16.85 wt.%; UO_2 = 0.12–0.47 wt.%), whereas CD_Q2 is composed of high-LREE and low-Th contents (Y_2O_3 = 1.71–2.33 wt.%; ThO_2 = 3.75–9.77 wt.%; UO_2 = 0.06–0.39 wt.%; Table 5 and Supplementary Data Table S4). These two compositional domains yielded distinct age populations at 496 ± 7 Ma (n = 18; MSWD = 1.4) and 439 ± 13 Ma (n = 5; MSWD = 0.30), respectively (Fig. 12i).

Monazite grains in sample G55 are fine to medium-sized (~60 µm–120µm), subhedral to anhedral and occur as inclusions within K-feldspar, quartz and biotite in the matrix (Fig. 12j, k). The CD_Q1 (Y_2O_3 = 2.33–3.22 wt.%; ThO_2 = 6.95–8.02 wt.%; UO_2 = 0.09–0.36 wt.%) and CD_Q2 (Y_2O_3 = 1.98–2.49 wt.%; ThO_2 = 2.92–5.36 wt.%; UO_2 = 0.18–0.87 wt.%) monazite domains show distinct compositions and yielded ages of 469 ± 16 Ma (n = 3; MSWD = 0.67) and 427 ± 17 Ma (n = 5; MSWD = 0.74), respectively (Fig. 12l; Table 5 and Supplementary Data Table S4).

8. Discussion

8. 1. Metamorphic evolution of gneisses from the Mikir Hills

The metamorphic *P–T* evolution of pelitic and quartzo-feldspathic gneisses of the Mikir Hills area is established based on mineral paragenesis, mineral chemistry (including garnet zoning patterns), conventional thermobarometry and pseudosection modelling (Fig. 13a). Mesoscale structures and microtextures indicate that the gneisses have experienced three stages of deformation (D_1, D_2 and D_3), and three episodes of metamorphism (M_{PR}, M_P and M_{PP}). In pelitic gneisses, the curved inclusion trails (Bt_1 + Qz + Ilm + Rt ± Pl_1) in garnet demarcate the relict S_1 foliation, indicating that the stability of garnet core formed during prograde metamorphism (M_{PR}) and postdates D_1 deformation. During prograde metamorphism, the gneisses witnessed significant melting that resulted in the development of melanocratic and leucocratic layers and melt migration microtextures with stability of peak metamorphic assemblage (i.e., Grt_{core} + Kfs + Sil_1 + Bt_2 + Pl_2 + Qz + Ilm ± Rt). Due to high-temperature (migmatised) peak metamorphism, the signatures of prograde metamorphism were mostly obliterated. However, melt-reintegration phase equilibria modelling suggested that the prograde metamorphism occurred in the garnet and sillimanite stability field. This is indicated by the

stability of sillimanite (Sil_1), K-feldspar and plagioclase (Pl_2). Pseudosection modelling suggests that the peak metamorphic assemblages in samples G52 and G53 are stable in the *P–T* conditions of 8.0–8.6 kbar at 768–780 °C and 5.8–7.5 kbar at 715–750 °C, respectively (Figs. 9a–d and 13a). These results broadly corroborate the results obtained using conventional thermobarometry (Table 3). The post-peak metamorphism stabilized cordierite-quartz and cordierite-spinel symplectites at *P–T* conditions of 4.0–5.0 kbar at 720–765 °C and 2.0–3.8 kbar at 640–730 °C, respectively. Overall, the results of pseudosection modelling, including the melt reintegration approach, determined a clockwise *P–T* path for migmatised pelitic gneisses (G52 and 53) and a cooling path for migmatised quartzo-feldspathic gneiss (G55) in the Mikir Hills region (Figs. 2, 9 and 10). The clockwise *P–T* trajectory of pelitic gneisses involves migmatisation-related peak metamorphism followed by isothermal decompression.

For quartzo-feldspathic gneisses, pseudosection modelling suggests that the peak metamorphic assemblage (i.e., garnet + K-feldspar + plagioclase + biotite + ilmenite + quartz + melt) is stable over a wide range of *P–T* conditions at 3.0 to > 12.0 kbar and 670–800 °C (Fig. 10). However, the compositional isopleths indicate that these equilibrated at much lower *P–T* conditions of 3.8–4.6 kbar and 590–650 °C (Fig. 10). These results are consistent with those *P–T* conditions (6.7–7.4 kbar and 601–658 °C; Table 3) calculated using conventional thermobarometry. The *P–T* estimates on quartzo-feldspathic gneisses broadly match the peak and post-peak metamorphic conditions of pelitic gneisses (Fig. 13a). Therefore, it is evident that both gneisses affected by common metamorphic episodes.

The preservation of weakly retrogressed upper amphibolite to granulite facies assemblages indicates substantial melt loss from the system during the metamorphism of migmatised pelitic gneisses (cf. White and Powell, 2002). In general, the large-scale crustal melting can be explained either by prograde heating (crustal thickening and volatile-induced melting; Fig. 14a) or decompression melting mechanisms (Harris and Inger, 1992; Harris and Massey, 1994; Patiño Douce and Harris, 1998; Harris et al., 2004; Searle et al., 2009; Streule et al., 2010; Groppo et al., 2012). The textural relations and phase equilibria modelling results suggest that the melting in pelitic gneisses occurred due to the biotite melting (reaction 1) reaction. The melting in gneisses would have been triggered mainly by prograde heating with a minor effect of isothermal decompression (Streule et al., 2010; Groppo et al., 2012).

Previous studies were mainly focused on the metamorphic evolution of western and central parts of the AMGC (Chatterjee et al., 2007, 2011; Dwivedi et al., 2020), and *P–T* paths reconstructed from these studies are correlated with the *P–T–t* paths obtained from this study (Fig. 13b). The garnet-orthopyroxene granulites exposed in western AMGC (Garo-Goalpara Hills) recorded a counterclockwise *P–T* path (Chatterjee et al., 2007). In contrast, garnet-cordierite-sillimanite-bearing pelitic granulites from central AMGC (Umpretha and Sonapahar areas) show clockwise *P–T* paths under near-isothermal decompression conditions (Chatterjee et al., 2011; Dwivedi et al., 2020). The metamorphic conditions obtained for pelitic gneiss (in this study) are broadly similar to the *P–T* conditions derived from pelitic granulites in the Umpretha area (Chatterjee et al., 2011) but show a significant variation as compared to the Sonapahar pelitic granulites, where Dwivedi et al. (2020) obtained extreme temperature conditions (>820 °C) using average *P–T* method. Their study would have overestimated the *P–T* conditions as the average *P–T* method ignores the activity corrections for melt components (cf. Dasgupta et al., 2009; Sorcar et al., 2014).

8.2. Interpretation of zircon-monazite age data and timing of migmatization

The zircon ages from the Mikir Hills migmatised pelitic (G53) and quartzo-feldspathic (G55) gneisses yielded Concordia age of 1647 ± 11 (±*16*) Ma (*n* = 3; MSWD = 1.3) and an upper intercept age of 1683 ± 44 (±*45*) Ma (MSWD = 1.4) for sample G53 (Fig. 11a). Sample G55 yielded slightly lower Concordia and upper intercept ages of 1590 ± 7 (±*14*) Ma (MSWD = 1.0) and 1613 ± 19 (±*22*) Ma (MSWD = 1.3), respectively (Fig. 11b; Table 5). These zircon grains are characterized by Th/U ratios of 0.59–1.82, indicating that the zircon growth occurred in magmatic conditions (Th/U > 0.1; Hoskin and Schaltegger, 2003; Rubatto, 2017; Yakymchuck et al., 2018). According to their study, metamorphic zircons mostly show Th/U ratios < 0.1, primarily controlled by the presence other Th-bearing minerals such as monazite and xenotime. Therefore, the ages obtained from oscillatory zircon cores are interpreted to represent the inherited igneous components of their Mesoproterozoic protolith (ca. 1647–1590 Ma). The Mesoproterozoic protolith components in the Mikir Hills, although preserved as relict zircon cores, can be temporally equivalent to the Mesoproterozoic high-grade granulites in the western AMGC near Garo-Goalpara Hills (Fig. 13c–e).

Monazite dating of two pelitic gneisses yielded two weighted mean age groups at 1058 ± 35 Ma and 480 ± 8 Ma to 467 ± 16 Ma (Fig. 12). The older age population (1058 ± 35 Ma) obtained from monazite cores (CD_P1) may plausibly attest to a thermal event associated with 1.1 Ga granite magmatism (Yin et al., 2010) in the Mikir Hills region. Low Y + HREE and low Th/U ratios in CD_P1 possibly indicate that this domain is formed in low-grade metamorphic conditions (cf. Zi et al., 2023) from a protolith that is poorer in Y + HREE budget. We speculate that the later high-grade migmatization event would have largely obliterated the mineralogical growth related to ~1058 ± 35 Ma metamorphism. Significant negative Y and Eu anomalies and high Th/U ratios (Supplementary Data Fig. S2) in younger monazite domains infer that these monazites were formed in equilibrium with a high abundance of garnet and plagioclase in high-temperature metamorphic conditions, involving partial melting. During partial melting, Th and U partitioned into the melt (Keppler and Wyllie, 1990), and the monazites forming from this melt preferentially sequester Th in its chemical composition (Bea and Montero, 1999; Xing et al., 2013), resulting in high Th/U ratios. We interpret that this episode of metamorphism crossed the muscovite and biotite breakdown melting reactions, consistent with the petrographic observations and mineral paragenesis. Therefore, we relate the ~480 ± 7 Ma to 467 ± 16 Ma age population to the peak metamorphic conditions and migmatisation in pelitic gneisses. A similar age of 496 ± 7 Ma is obtained from high Y and Th domains of quartzo-feldspathic gneisses, indicating that these rocks experienced a common partial melting event along with pelitic gneisses during ~496–467 Ma.

Younger monazite domains in four samples, with ages between 439 ± 13 Ma and 427 ± 17 Ma, are interpreted to represent the timing of fluid-mediated regrowth of monazites. If monazite grains are regrown under fluid-mediated conditions, the newly formed domains generally crosscut the original zoning patterns along dissolution–precipitation fronts and usually develop patchy monazite domains (Williams et al., 2006; Putnis, 2009; Hetherington et al., 2010;

765 Hurai et al., 2015). Similar patchy textures are observed in CD_Q2 monazite domains, which are
766 depleted in Th, Pb and HREE concentrations relative to CD_Q1 monazite domains (Fig. 12 and
767 Supplementary Data Fig. S2; Supplementary Data Table S4). Therefore, the younger population
768 (439–427 Ma) obtained from these disseminated patchy zones represent the timing of the
769 regrowth of monazites in response to fluid infiltration.

770 A large dataset of U–Pb zircon ages and U-Th-total Pb monazite ages are available from
771 western, central and eastern parts of the AMGC, and these ages are correlated with the ages
772 yielded in this study (Fig. 13c–e). Previous studies on AMGC gneisses identified four major age
773 populations at ~1670–1520 Ma, ~1430–1350 Ma, ~1140–1000 Ma and ~520–480 Ma (Fig. 13c–
774 e). In addition, the Assam-Meghalaya gneissic complex recorded three episodes of granite
775 magmatism at ~1700–1470 Ma, ~1150–980 Ma and ~560–420 Ma (Fig. 13c–d). Although
776 geochronological data from gneisses of Mikir Hills (eastern AMGC) is scarce, Yin et al. (2010)
777 reported augen gneisses with an age range of 1628–1400 Ma, which are coeval with ages from
778 granites in the Mikir Hills region. These plutons include Panbari-Geleki, Kuthori and Dallamara
779 granites, yielding U–Pb ages of 1644 ± 33 Ma, 1599 ± 17 Ma and 1550 ± 25 Ma, respectively
780 (Gogoi et al., 2019). In summary, the 1647–1590 Ma zircon ages obtained from this study are
781 corresponding to the timing of emplacement of igneous protolith or high-grade metamorphism in
782 the Mikir Hills region, whereas younger ages (496–467 Ma) are related to the timing of
783 migmatisation in the eastern AMGC (Fig. 14a). The timing of migmatisation was coeval with the
784 emplacement of various granitoids, including Nongpoh (507 ± 7 Ma), Krydem (513 ± 9 Ma) and
785 South Khasi (517 ± 9 Ma) plutons in the central AMGC (Kumar et al., 2017), and Kathalguri
786 (516 ± 3 Ma; Majumdar and Dutta, 2016) and Kaziranga Park (529 ± 6 Ma; Kumar et al., 2017)
787 plutons in the Mikir Hills regions (Fig. 14a).

788

789 *8.3. Significance of Meso- to Neoproterozoic tectonism in the Mikir Hills*

790

791 The 1596 ± 15 Ma monazite age reported from metapelites in Garo Hills (western
792 AMGC) have been interpreted to represent the timing of granulite facies metamorphism and are
793 correlated with a collisional event associated with the amalgamation of North Indian Block
794 (NIB) and South Indian Block (SIB) along Central Indian Tectonic Zone (CITZ) (Chatterjee et
795 al., 2007; Chatterjee, 2017). According to these authors, the southward subduction of the oceanic
796 lithosphere underneath the SIB has led to the formation of an island arc. The sediments deposited
797 in the back-arc basin witnessed intense heating and metamorphism, followed by isobaric cooling
798 and the formation of granulites exhibiting anti-clockwise *P–T* paths (Chatterjee et al., 2007).
799 Although Mesoproterozoic high-grade metamorphism is unidentified in the Mikir Hills region,
800 the present study shows the occurrence of 1647–1590 Ma magmatic zircons in pelitic and
801 quartzo-feldspathic gneisses. These ages overlap with the timing of ubiquitous granite
802 magmatism (i.e., 1674–1561 Ma; Gogoi et al., 2019) in the Mikir Hills. The inheritance of
803 similar zircon ages (i.e., 1704–1520 Ma) in orthogneisses and pelitic gneisses from central
804 AMGC (Yin et al., 2010; Dwivedi et al., 2023) and in Mikir Hills (1647–1590 Ma; this study)
805 infers a regionally extensive ~1600 Ma tectono-magmatic event in northeast India. Previous
806 geochronological studies suggest that Western Australia and East Antarctica lack ~1600 Ma

tectonic imprint but record a strong ~1126–968 Ma tectonism in the Leeuwin, Mullingarra, and Northampton Complexes of Western Australia and Prince Charles Mountains–Prydz Bay region of East Antarctica (Figs. 1 and 14b; Myers, 1990).

The weakly preserved ~1058 ± 35 Ma tectonic imprint in the Mikir Hills can be corroborated with similar tectonothermal events recorded in various parts of AMGC. Chatterjee et al. (2007) reported ~1078 ± 31 Ma for monazite cores from metapelites in Sonapahar (central AMGC; Fig. 13d). However, they have not interpreted the tectonic significance of this event. Later, Yin et al. (2010) reported ~1129–1039 Ma magmatism near Guwahati (central AMGC) and from the northern Mikir Hills using U–Pb zircon geochronology. In eastern India, the island-arc magmatism between the Eastern Ghats belt and Rayner Province (East Antarctica) resulted in UHT metamorphism at ~1030–970 Ma (Fig. 14a; Bose et al., 2022). This thermal imprint is reported from other nearby crustal domains in India (i.e., Bastar Craton, Singhbhum Craton, Dharwar Craton and central Indian tectonic zone) (Bose et al., 2022). The ~1100–1000 Ma tectonothermal episode recorded in eastern India can be correlated with temporally equivalent felsic magmatism and associated metamorphism in Western Australia and East Antarctica (Wang et al., 2008; Grew et al., 2012; Spreitzer et al., 2021). A prolonged and complex history of high-grade metamorphism is recorded in the basement complexes of Western Australia at 1090–1020 Ma (Fig. 14b). Similarly, East Antarctica preserved significant Grenvillian ages and was devoid of Mesoproterozoic tectono-metamorphic events (Fig. 14b). The orthogneisses in the Larsemann Hills (Prince Charles Mountain-Prydz Bay region) recorded magmatic episodes during 1126–968 Ma (Wang et al., 2008; Grew et al., 2012) and high-pressure metamorphism at ~911 ± 9 Ma (Spreitzer et al., 2021). The geochronological correlations among Western Australia, East Antarctica and Eastern India suggest that these land masses were juxtaposed and shared a common tectono-thermal history during Grenvillian Orogeny (Fig. 14b; Collins and Pisarevsky, 2005; Boger, 2011; Ksienzyk et al., 2012; Markwitz et al., 2017). Although these correlations suggest that the Mikir Hills region shared a common tectonic history with Western Australia and East Antarctica, the Mikir Hills would have been located distantly from these crustal units. As a result, the Mikir Hills region (this study) and central AMGC (Chatterjee, 2017) recorded a weak imprint of ~1100–1000 Ma event.

8.4. Late Neoproterozoic magmato-metamorphic events and its significance in the assembly of eastern Gondwana

Late Neoproterozoic Circum-Indian orogens are helpful in paleogeographic reconstructions of Supercontinent Gondwana. These orogens are typically regarded as collisional belts resulting from final amalgamation between India-Western Australia-East Antarctica (eastern Gondwana) and Africa-South America (western Gondwana) continental blocks (Collins and Pisarevsky, 2005 and references therein). A compilation of the *P–T* paths obtained from Prydz Bay region (East Antarctica)–Western Australia–AMGC (northeast India) are provided in Fig. 13b, and a summary of tectono-magmatic episodes is given in Fig. 14. The Leeuwin Complex in Western Australia preserved the youngest high-grade metamorphic event at ~522 ± 2 Ma (Collins, 2003) and ~526 ± 12 Ma (Markwitz et al., 2017), indicating the tectonic event

associated with the assembly of Gondwana supercontinent (Boger, 2011). The mafic granulites from Larsemann Hills recorded ultrahigh temperature metamorphism at ~530 Ma, marking the signatures associated with Gondwana assembly in East Antarctica (Liu et al., 2007; Wang et al., 2022). Similar ~545–530 Ma granulite facies metamorphism with a clockwise *P–T* was reported from metapelites in the Prince Charles Mountain-Prydz Bay region, East Antarctica (Boger and Wilson, 2005; Liu et al., 2013).

A number of studies have described Late Neoproterozoic metamorphic events in the southern India and Eastern Ghats (~550–450 Ma; Mezger and Cosca, 1999; Dobmeier and Raith, 2003; Plavsa et al., 2015; Sheikh et al., 2020), while limited information has been obtained from northeast India, particularly the Assam-Meghalaya gneissic complex. Kumar et al. (2017) reported a strong Late Neoproterozoic granite magmatism (~529–515 Ma) from the Mikir Hills region (eastern AMGC). As shown in the present study, various rocks of Mikir Hills preserve the evidence for deformation (minimum two stages), high-grade peak metamorphism (5.3–8.6 kbar and 730–780 °C) and partial melting during 496–467 Ma. This metamorphic history (this study) from Mikir Hills is reported for the first time and is similar to the younger tectonothermal evolution (Chatterjee et al., 2007, 2011; Dwivedi, 2011, 2020) reported from high-grade pelitic gneisses of the central AMGC, indicating that these domains shared a common tectonometamorphic history during Late Neoproterozoic. Further, the clockwise *P–T* paths from pelitic gneisses (in the present study) fall within the thermal gradients of 75 °C/km (High-T peak metamorphism) and 150 °C/km (Fig. 13b; post-peak isothermal decompression), which is characteristic of a Proterozoic collisional or accretionary orogen (Kelsey and Hand, 2015) related to the East Gondwana supercontinent assembly.

This study confirms the eastern extension of the Pan-African orogenic front, which is spread for ~300 km between central and eastern AMGC. The dominance of Late Neoproterozoic reworking of the Paleo- to Mesoproterozoic crust and high-grade metamorphism suggest that the eastern AMGC represent the lower part of an active convergent margin. The contractional deformation at ~550–450 Ma led to crustal thickening associated with the collision (Kuunga Orogeny) between India-Australia-Antarctica cratons. The possible magmatic underplating beneath the Mesoproterozoic crust would have resulted in prograde partial melting of pelitic and quartzo-feldspathic gneisses (M_{PR} to M_P), followed by isothermal decompression event (M_P to M_{PP}) during orogenic collapse (Fig. 14a). Post-collisional crustal thinning accompanied by the emplacement of A-type granitoids in the AMGC (Fig. 14a; cf. Majumdar and Dutta, 2016) is likely to have played a significant role in the exhumation of the Mikir Hills region (eastern AMGC) after the cessation of compressional tectonics leading to the assembly of east Gondwana supercontinent.

9. Conclusions

The conclusions drawn from this study are summarized below:

(1) The migmatised pelitic and quartzo-feldspathic gneisses of the Mikir Hills region of the eastern Assam-Meghalaya gneissic complex provide robust examples of regional high-grade

metamorphism in accretionary-collisional belt developed during the assembly of eastern Gondwana supercontinent.

(2) The new results obtained using phase equilibria modelling indicate that the pelitic and quartzo-feldspathic gneisses of Mikir Hills have experienced peak metamorphic conditions of 8.0–8.6 kbar at 768–780 °C and 3.8–4.6 kbar at 590–650 °C, respectively.

(3) The 496 ± 7 Ma to 467 ± 16 Ma monazite ages obtained in this study are interpreted to represent the timing of regional migmatisation in the Mikir Hills region (eastern AMGC).

(4) Zircons from pelitic and quartzo-feldspathic gneisses preserved relics of Mesoproterozoic igneous protolith ages (1647 ± 11 Ma to 1590 ± 7 Ma) that are equivalent to granulite facies rocks present in the western AMGC. The ~1058 ± 35 Ma age identified in monazites possibly represents the tectonism associated with the amalgamation of India with Western Australia-East Antarctica during the Rodinia assembly.

(5) The dominance of Late Neoproterozoic migmatisation and magmatism indicate that the Mikir Hills regions represent an active convergent margin, which evolved as a hot (Kuunga) orogen during the assembly of eastern Gondwana. The Late Neoproterozoic tectonothermal events related to the AMGC are broadly consistent with those observed in Western Australia and East Antarctica.

Acknowledgements

This manuscript is a part of the doctoral research work of Rahul Nag at the Indian Institute of Technology Bombay. Rahul's research work is supported by the Prime Minister's Research Fellows (PMRF) scheme from the Ministry of Education, New Delhi, Government of India (PMRF ID: 1300753). Fieldwork and laboratory studies were financially supported by the Science and Engineering Research Board (SERB, Govt. of India) core research grant (CRG/2019/000812) to N. Prabhakar. Mineral and monazite analyses were performed using the SERB-funded EPMA National Facility at the Department of Earth Sciences, IIT Bombay (IRPHA grant no. IR/S4/ESF-16/2009). Prabhakar acknowledges the core research grant (file no. CRG/2019/000812) for the financial support given for laboratory analysis. Javed M. Shaikh is thanked for his help with EPMA analysis. We thank two anonymous reviewers for their useful comments that helped improved this manuscript. The Authors also acknowledge editorial handling of Prof. M. Santosh and Vinod Samuel.

References

Ashworth, J.R., McLellan, E.L., 1985. Textures. In: Ashworth, J.R. (eds) Migmatites. Springer, Boston, MA, pp. 180-203.

Bidyananda, M., Deomurari, M.P., 2007. Geochronological constraints on the evolution of Meghalaya massif, northeastern India: an ion microprobe study. Curr. Sci. 93, 1620-1623.

Banerjee, A., Sequeira, N., Cogné, N., Prabhakar, N., Bhattacharya, A., Ao, S., 2022. Early Neoproterozoic Tectonics in the Godhra–Chhota Udepur Sector: Evidence for Two-Stage Accretion in the Great Indian Proterozoic Fold Belt. Lithosphere (Special 8), 9322892.

Bea, F., Montero, P., 1999. Behavior of accessory phases and redistribution of Zr, REE, Y, Th, and U during metamorphism and partial melting of metapelites in the lower crust: an example from the Kinzigite Formation of Ivrea-Verbano, NW Italy. Geochim. Cosmochim. Acta. 63, 1133-1153.

Bhattacharya, A., Mazumdar, A.C., Sen, S.K., 1988. Fe-Mg mixing in cordierite; constraints from natural data and implications for cordierite-garnet geothermometry in granulites. Am. Mineral. 73, 338-344.

Bilham, R., England, P., 2001. Plateau 'pop-up' in the great 1897 Assam earthquake. Nature 410(6830), 806-809.

Biswas, S., Grasemann, B., 2005. Quantitative morphotectonics of the southern Shillong plateau (Bangladesh/India). Aust. J. Earth Sci. 97, e93.

Boger, S.D. and Wilson, C.J.L., 2005. Early Cambrian crustal shortening and a clockwise P–T–t path from the southern Prince Charles Mountains, East Antarctica: implications for the formation of Gondwana. J. Metamorph. Geol. 23, 603-623.

Boger, S.D., 2011. Antarctica—before and after Gondwana. Gondwana Res. 19, 335-371.

Boger, S.D., Maas, R., Pastuhov, M., Macey, P.H., Hirdes, W., Schulte, B., Fanning, C.M., Ferreira, C.A.M., Jenett, T., Dallwig, R., 2019. The tectonic domains of southern and western Madagascar. Precambr. Res. 327, 144-175.

Bose, S., Dasgupta, S., 2018. Eastern Ghats Belt, Grenvillian-age tectonics and the evolution of the Greater Indian Landmass: a critical perspective. J. Indian Inst. Sci. 98, 345-363.

Bose, S., Sorcar, N., Das, K., Ganguly, P., Mukherjee, S., 2022. Pulsed tectonic evolution in long-lived orogenic belts: An example from the Eastern Ghats Belt, India. Precambr. Res. 369, 106522.

Borah, P., Hazarika, P., Mazumdar, A.C., Rabha, M., 2019. Monazite and xenotime U–Th–Pb_{total} ages from basement rocks of the (central) Shillong–Meghalaya Gneissic Complex, Northeast India. J. Earth Sys. Sci. 128, 1-20.

Braun, I., Raith, M., Kumar, G.R., 1996. Dehydration-melting phenomena in leptynitic gneisses and the generation of leucogranites: a case study from the Kerala khondalite belt, southern India. J. Petrol. 37, 1285-1305.

Bruguier, O., Bosch, D., Pidgeon, R.T., Byrne, D.R., Harris, L.B., 1999. U-Pb chronology of the Northampton Complex, Western Australia - evidence for Grenvillian sedimentation, metamorphism and deformation and geodynamic implications. Contrib. Mineral. Petrol. 136, 258–272.

Carson, C.J., Powell, R., Wilson, C.J.L., Dirks, P.H.G.M., 1997. Partial melting during tectonic exhumation of a granulite terrane: an example from the Larsemann Hills, East Antarctica. J. Metamorph. Geol. 15, 105-126.

Chatterjee, N., 2017. Constraints from monazite and xenotime growth modelling in the Mn CKFMASH-PYCe system on the P–T path of a metapelite from Shillong-Meghalaya Plateau: implications for the Indian shield assembly. J. Metamorph. Geol. 35, 393-412.

Chatterjee, N., Bhattacharya, A., Duarah, B.P., Mazumdar, A.C., 2011. Late Cambrian reworking of Paleo-Mesoproterozoic granulites in Shillong-Meghalaya gneissic complex (Northeast India): evidence from P-T pseudosection analysis and monazite chronology and implications for East Gondwana assembly. The J. Geol. 119, 311-330.

Chatterjee, N., Mazumdar, A.C., Bhattacharya, A., Saikia, R.R., 2007. Mesoproterozoic granulites of the Shillong–Meghalaya Plateau: evidence of westward continuation of the Prydz Bay Pan-African suture into Northeastern India. Precambr. Res. 152, 1-26.

Chen, L., Wang, W., Liu, X., Zhao, Y., 2018. Metamorphism and zircon U–Pb dating of high-pressure pelitic granulites from glacial moraines in the Grove Mountains, East Antarctica. Adv. Polar Sci. 29, 118-134.

Clarke, G.L., Powell, R., 1991. Decompressional coronas and symplectites in granulites of the Musgrave Complex, central Australia. J. Metamorph. Geol. 9, 441-450.

Collins, A.S., 2003. Structure and age of the northern Leeuwin Complex, Western Australia: constraints from field mapping and U–Pb isotopic analysis. Aust. J. Earth Sci. 50, 585-599.

Collins, A.S., Pisarevsky, S.A., 2005. Amalgamating eastern Gondwana: the evolution of the Circum-Indian Orogens. Earth-Sci. Rev. 71, 229-270.

Connolly, J.A., 2005. Computation of phase equilibria by linear programming: a tool for geodynamic modeling and its application to subduction zone decarbonation. Earth Planet. Sci. Lett. 236, 524-541.

Dasgupta, S., Chakraborty, S., Neogi, S., 2009. Petrology of an inverted Barrovian sequence of metapelites in Sikkim Himalaya, India: constraints on the tectonics of inversion. Am. J. Sci. 309, 43-84.

Deer, W.A., Howie, R.A., Zussman, J., 1992. An Introduction to The Rock-Forming Minerals. Essex. England, Longman Scientific and Technology, pp. 696.

994 Deshmukh, T., Prabhakar, N., Bhattacharya, A., Madhavan, K., 2017. Late Paleoproterozoic
995 clockwise P–T history in the Mahakoshal Belt, Central Indian Tectonic zone: implications
996 for Columbia supercontinent assembly. Precambr. Res. 298, 56-78.

997 Dey, S., Mitra, A., Nandy, J., Mondal, S., Topno, A., Liu, Y., Zong, K., 2019. Early crustal
998 evolution as recorded in the granitoids of the Singhbhum and Western Dharwar
999 Cratons. Earth's Oldest Rocks. 1, 741-792.

1000 Dharmapriya, P.L., Malaviarachchi, S.P., Santosh, M., Tang, L., Sajeev, K., 2015. Late-
1001 Neoproterozoic ultrahigh-temperature metamorphism in the Highland Complex, Sri Lanka.
1002 Precambr. Res. 271, 311-333.

1003 Diener, J.F.A., White, R.W., Powell, R., 2008. Granulite facies metamorphism and subsolidus
1004 fluid-absent reworking, Strangways Range, Arunta Block, central Australia. J. Metamorph.
1005 Geol. 26, 603-622.

1006 Dobmeier, C.J., Raith, M.M., 2003. Crustal architecture and evolution of the Eastern Ghats Belt
1007 and adjacent regions of India. Geol. Soc. London Spec. Publ. 206, 145-168.

1008 Dwivedi, S.B., 2011. Geodynamic evolution of Mesoproterozoic Granulites of Meghalaya:
1009 Evidence from Geothermobarometry, P-T Path and P-T Pseudosection. Mem. Geol. Soc.
1010 India 77, 85-101.

1011 Dwivedi, S.B., Pathak, P., Theunuo, K., Kumar, R.R., 2023. U–Pb SHRIMP zircon dating and
1012 geochemistry of metapelites from the Shillong Meghalaya Gneissic Complex, NE India:
1013 Implications for nature of protolith and tectonic setting. Geosys. Geoenviron. 2, 100161.

1014 Dwivedi, S.B., Theunuo, K., Kumar, R.R., 2020. Characterization and metamorphic evolution of
1015 Mesoproterozoic granulites from Sonapahar (Meghalaya), NE India, using EPMA
1016 monazite dating. Geol. Mag. 157, 1409-1427.

1017 Endo, T., Tsunogae, T., Santosh, M., Shaji, E., 2012. Phase equilibrium modeling of incipient
1018 charnockite formation in NCKFMASHTO and MnNCKFMASHTO systems: A case study
1019 from Rajapalaiyam, Madurai Block, southern India. Geosci. Front. 3, 801-811.

1020 Eremenco, N.A., Negi, B.S., Nasianov, M.V., Seregin, A.M., Despande, B.G., Sengupta, S.N.,
1021 Talukdar, S.N., Sastri, V.V., Sokaluv, I.P., Pavbukov, A.T., Datta, A.K., Raju, A.T.R.,
1022 1969. Tectonic map of India - Principles of preparation. Bull. ONGC. 6, 1–111.

1023 Evans, D.A., Sircombe, K.N., Wingate, M.T., Doyle, M., McCarthy, M., Pidgeon, R.T., Van
1024 Niekerk, H.S., 2003. Revised geochronology of magmatism in the western Capricorn
1025 Orogen at 1805–1785 Ma: Diachroneity of the Pilbara-Yilgarn collision. Aust. J. Earth Sci.
1026 50, 853-864.

1027 Evans, P., 1964. The tectonic framework of Assam. Geol. Soc. India. 5, 80-96.

1028 Fitzsimons, I.C.W., 1996. Metapelitic migmatites from Brattstrand Bluffs, East Antarctica-
1029 metamorphism, melting and exhumation of the mid crust. J. Petrol. 37, 395-414.

Fitzsimons, I.C.W., 2003. Proterozoic basement provinces of southern and southwestern Australia, and their correlation with Antarctica. Geol. Soc. London Spec. Publ. 206, 93-130.

Fritz, H., Abdelsalam, M., Ali, K.A., Bingen, B., Collins, A.S., Fowler, A.R., Ghebreab, W., Hauzenberger, C.A., Johnson, P.R., Kusky, T.M., Macey, P., 2013. Orogen styles in the East African Orogen: a review of the Neoproterozoic to Cambrian tectonic evolution. J. Afr. Earth Sci. 86, 65-106.

Ganguly, J., Chakraborty, S., Sharp, T.G., Rumble, D., 1996. Constraint on the time scale of biotite-grade metamorphism during Acadian orogeny from a natural garnet-garnet diffusion couple. Am. Mineral. 81, 1208-1216.

Ghosh, S., Bhalla, J. K., Paul, D.K., Sarkar, A., Bishul, P.K., Gupta, S.N., Chakraborty, S., 1991. Geochronology and geochemistry of graniteplutons from East Khasi Hills, Meghalaya. J. Geol. Soc. Ind. 37, 331–342.

Ghosh, S., Paul, D.K., Bhalla, J.K., Bishui, P.K., Gupta, S.N., Chakraborty, S., 1994. New Rb-Sr isotopic ages and geochemistry of granitoids from Meghalaya and their significance in middle- to late Proterozoic crustal evolution. Ind. Min. 48, 33–34.

Ghosh, S., Fallick, A.E., Paul, D.K., Potts, P.J., 2005. Geochemistry and origin of Neoproterozoic granitoids of Meghalaya, Northeast India: Implications for linkage with amalgamation of Gondwana supercontinent. Gondwana Res. 8, 421-432.

Gogoi, A., Majumdar, D., Cottle, J., Dutta, P., 2019. Geochronology and geochemistry of Mesoproterozoic porphyry granitoids in the northern Karbi Hills, NE India: Implications for early tectonic evolution of the Karbi Massif. J. Asian Earth Sci. 179, 65-79.

Gray, D.R., Foster, D.A., Meert, J.G., Goscombe, B.D., Armstrong, R., Trouw, R.A.J., Passchier, C.W., 2008. A Damara orogen perspective on the assembly of southwestern Gondwana. Geol. Soc. London Spec. Publ. 294, 257-278.

Grew, E.S., Carson, C.J., Christy, A.G., Maas, R., Yaxley, G.M., Boger, S.D., Fanning, C.M., 2012. New constraints from U–Pb, Lu–Hf and Sm–Nd isotopic data on the timing of sedimentation and felsic magmatism in the Larsemann Hills, Prydz Bay, East Antarctica. Precambr. Res. 206, 87-108.

Groppo, C., Rolfo, F., Indares, A., 2012. Partial melting in the Higher Himalayan Crystallines of Eastern Nepal: the effect of decompression and implications for the 'Channel Flow' model. J. Petrol. 53, 1057-1088.

Gupta, R.P., Sen, A.K., 1988. Imprints of the ninety-east ridge in the Shillong Plateau, Indian Shield. Tectonophysics 154, 335-341.

Harris, N., Massey, J., 1994. Decompression and anatexis of Himalayan metapelites. Tectonics 13, 1537-1546.

1066 Harris, N.B.W., Caddick, M., Kosler, J., Goswami, S., Vance, D., Tindle, A.G., 2004. The
1067 pressure–temperature–time path of migmatites from the Sikkim Himalaya. J. Metamorph.
1068 Geol. 22, 249-264.

1069 Harris, N.B.W., Inger, S., 1992. Trace element modelling of pelite-derived granites. Contrib.
1070 Mineral. Petrol. 110, 46-56.

1071 Henry, D.J., Guidotti, C.V., Thomson, J.A., 2005. The Ti-saturation surface for low-to-medium
1072 pressure metapelitic biotites: Implications for geothermometry and Ti-substitution
1073 mechanisms. Am. Mineral. 90, 316-328.

1074 Hensen, B.J., 1971. Theoretical phase relations involving cordierite and garnet in the system
1075 MgO-FeO-Al_2O_3-SiO_2. Contrib. Mineral. Petrol. 33, 191-214.

1076 Hetherington, C.J., Harlov, D.E., Budzyń, B., 2010. Experimental metasomatism of monazite
1077 and xenotime: mineral stability, REE mobility and fluid composition. Mineral. Petrol. 99,
1078 165-184.

1079 Hoffer, E., 1976. The reaction sillimanite+ biotite+ quartz ⇌ cordierite+ K-feldspar+ H_2O and
1080 partial melting in the system K_2O-FeO-MgO-Al_2O_3-SiO_2-H_2O. Contrib. Mineral.
1081 Petrol. 55, 127-130.

1082 Hoskin, P.W., Schaltegger, U., 2003. The composition of zircon and igneous and metamorphic
1083 petrogenesis. Rev. Mineral. Geochem. 53, 27-62.

1084 Holdaway, M.J., 2000. Application of new experimental and garnet Margules data to the garnet-
1085 biotite geothermometer. Am. Mineral. 85, 881-892.

1086 Holland, T.J.B., Powell, R.T.J.B., 1998. An internally consistent thermodynamic data set for
1087 phases of petrological interest. J. Metamorph. Geol. 16, 309-343.

1088 Horstwood, M.S., Košler, J., Gehrels, G., Jackson, S.E., McLean, N.M., Paton, C., Pearson, N.J.,
1089 Sircombe, K., Sylvester, P., Vermeesch, P., Bowring, J.F., 2016. Community-derived
1090 standards for LA-ICP-MS U-(Th)-Pb geochronology–Uncertainty propagation, age
1091 interpretation and data reporting. Geostand. Geoanalytical Res. 40, 311-332.

1092 Hoskin, P.W.O., Black, L.P., 2000. Metamorphic zircon formation by solid-state recrystallization
1093 of protolith igneous zircon. J. Metamorph. Geol. 18, 423-439.

1094 Hrushikesh, H., Prabhakar, N., Bhattacharya, A., 2019. Mesoproterozoic P–T–t–d history in the
1095 Vinjamuru domain, Nellore schist belt (SE India), and implications for SE India–East
1096 Antarctica correlation. Precambr. Res. 327, 273-295.

1097 Hurai, V., Paquette, J.L., Lexa, O., Konečný, P., Dianiška, I., 2015. U-Pb-Th geochronology of
1098 monazite and zircon in albitite metasomatites of the Rožňava-Nadabula ore field (Western
1099 Carpathians, Slovakia): implications for the origin of hydrothermal polymetallic siderite
1100 veins. Mineral. Petrol. 109, 519-530.

1101 Jercinovic, M.J., Williams, M.L., 2005. Analytical perils (and progress) in electron microprobe
1102 trace element analysis applied to geochronology: Background acquisition, interferences,
1103 and beam irradiation effects. Am. Mineral. 90, 526-546.

1104 Jiang, W.C., Li, H., Evans, N.J., Wu, J.H., 2019. Zircon records multiple magmatic-
1105 hydrothermal processes at the giant Shizhuyuan W–Sn–Mo–Bi polymetallic deposit, South
1106 China. Ore Geol. Rev. 115, 103160.

1107 Jöns, N., Schenk, V., 2011. The ultrahigh temperature granulites of southern Madagascar in a
1108 polymetamorphic context: implications for the amalgamation of the Gondwana
1109 supercontinent. Eur. J. Mineral. 23, 127-156.

1110 Kelsey, D.E., Hand, M., 2015. On ultrahigh temperature crustal metamorphism: phase equilibria,
1111 trace element thermometry, bulk composition, heat sources, timescales and tectonic
1112 settings. Geosci. Front. 6, 311-356.

1113 Kelsey, D.E., Hand, M., Clark, C., Wilson, C.J.L., 2007. On the application of in situ monazite
1114 chemical geochronology to constraining P–T–t histories in high-temperature (> 850° C)
1115 polymetamorphic granulites from Prydz Bay, East Antarctica. J. Geol. Soc. 164, 667-683.

1116 Keppler, H., Wyllie, P.J., 1990. Role of fluids in transport and fractionation of uranium and
1117 thorium in magmatic processes. Nature 348(6301), 531-533.

1118 Korhonen, F.J., Brown, M., Clark, C., Bhattacharya, S., 2013. Osumilite–melt interactions in
1119 ultrahigh temperature granulites: Phase equilibria modelling and implications for the P–T–t
1120 evolution of the Eastern Ghats Province, India. J. Metamorph. Geol. 31, 881-907.

1121 Ksienzyk, A.K., Jacobs, J., Boger, S.D., Košler, J., Sircombe, K.N., Whitehouse, M.J., 2012. U–
1122 Pb ages of metamorphic monazite and detrital zircon from the Northampton Complex:
1123 evidence of two orogenic cycles in Western Australia. Precambr. Res. 198, 37-50.

1124 Kumar, S., 1990. Petrochemistry and geochronology of pink granite from Songsak, east Garo
1125 Hills, Meghalaya. J. Geol. Soc. Ind. 35, 39–45.

1126 Kumar, S., Rino, V., Hayasaka, Y., Kimura, K., Raju, S., Terada, K., Pathak, M., 2017.
1127 Contribution of Columbia and Gondwana Supercontinent assembly- and growth-related
1128 magmatism in the evolution of the Meghalaya Plateau and the Mikir Hills, Northeast India:
1129 Constraints from U-Pb SHRIMP zircon geochronology and geochemistry. Lithos 277, 356-
1130 375.

1131 Kuribara, Y., Tsunogae, T., Takamura, Y., Tsutsumi, Y., 2019. Petrology, geochemistry, and
1132 zircon U-Pb geochronology of the Zambezi Belt in Zimbabwe: Implications for terrane
1133 assembly in southern Africa. Geosci. Front. 10, 2021-2044.

1134 La Roche, R.S., Gervais, F., Tremblay, A., Crowley, J.L., Ruffet, G., 2015. Tectono-
1135 metamorphic history of the eastern Taureau shear zone, Mauricie area, Québec:
1136 Implications for the exhumation of the mid-crust in the Grenville Province. Precambr.
1137 Res. 257, 22-46.

1138 Lanari, P., Vidal, O., De Andrade, V., Dubacq, B., Lewin, E., Grosch, E.G., Schwartz, S., 2014.
1139 XMapTools: A MATLAB©-based program for electron microprobe X-ray image
1140 processing and geothermobarometry. Comput. Geosci. 62, 227-240.

1141 Liu, X., Hu, J., Zhao, Y., Lou, Y., Wei, C., Liu, X., 2009. Late Neoproterozoic/Cambrian high-
1142 pressure mafic granulites from the Grove Mountains, East Antarctica: P–T–t path,
1143 collisional orogeny and implications for assembly of East Gondwana. Precambr. Res. 174,
1144 181-199.

1145 Liu, X., Sun, L., Xie, Z., Yin, X., Zhu, R., Wang, Y., 2007. A preliminary record of the historical
1146 seabird population in the Larsemann Hills, East Antarctica, from geochemical analyses of
1147 Mochou Lake sediments. Boreas 36, 182-197.

1148 Liu, X., Zhao, Y., Hu, J., 2013. The c. 1000–900 Ma and c. 550–500 Ma tectonothermal events
1149 in the Prince Charles Mountains–Prydz Bay region, East Antarctica, and their relations to
1150 supercontinent evolution. Geol. Soc. London Spec. Publ. 383, 95-112.

1151 Ludwig, K.R., 2003. Isoplot 3.00: a geochronological toolkit for Microsoft Excel. Berkeley
1152 Geochronology Center Spec. Publ. 4, pp. 70.

1153 Mahan, K.H., Goncalves, P., Williams, M.L., Jercinovic, A.M., 2006. Dating metamorphic
1154 reactions and fluid flow: Application to exhumation of high-P granulites in a crustal-scale
1155 shear zone, western Canadian Shield. J. Metamorph. Geol. 24, 193-217.

1156 Majumdar, D., Dutta, P., 2016. Geodynamic evolution of a Pan-African granitoid of extended
1157 Dizo Valley in Karbi Hills, NE India: evidence from geochemistry and isotope geology. J.
1158 Asian Earth Sci. 117, 256-268.

1159 Mange, M.A., Morton, A.C., 2007. Geochemistry of heavy minerals. Developments in
1160 Sedimentology 58, 345-391.

1161 Markwitz, V., Kirkland, C.L., Evans, N.J., 2017. Early Cambrian metamorphic zircon in the
1162 northern Pinjarra Orogen: Implications for the structure of the West Australian Craton
1163 margin. Lithosphere 9, 3-13.

1164 Matthews, J.A., 2013. Impact of accessory minerals on the distribution of trace elements in the
1165 continental crust: an integrated petrologic and phase equilibria modeling study of
1166 migmatites. Ph. D. Thesis. Colorado School of Mines, 236 pp.

1167 Mazumdar, S.K., 1976. A summary of the Precambrian geology of the Khasi Hills,
1168 Meghalaya. Geol. Surv. India Misc. Publ. 23, 311-334.

1169 Meert, J.G., 2003. A synopsis of events related to the assembly of eastern
1170 Gondwana. Tectonophysics 362, 1-40.

1171 Meert, J.G., Lieberman, B.S., 2008. The Neoproterozoic assembly of Gondwana and its
1172 relationship to the Ediacaran–Cambrian radiation. Gondwana Res. 14, 5-21.

1173 Merdith, A.S., Williams, S.E., Müller, R.D., Collins, A.S., 2017. Kinematic constraints on the
1174 Rodinia to Gondwana transition. Precambr. Res. 299, 132-150.

1175 Merlet, C., 1992. Quantitative Electron Probe Microanalysis: New Accurate Φ (ρz) Description.
1176 In: Boekestein, A., Pavićević, M.K. (Eds.), Electron Microbeam Analysis. Mikrochim.
1177 Acta, Springer, Vienna, pp. 107-115.

1178 Mezger, K., Cosca, M.A., 1999. The thermal history of the Eastern Ghats Belt (India) as revealed
1179 by U–Pb and $^{40}Ar/^{39}Ar$ dating of metamorphic and magmatic minerals: implications for the
1180 SWEAT correlation. Precambr. Res. 94, 251-271.

1181 Milord, I., Sawyer, E.W., Brown, M., 2001. Formation of diatexite migmatite and granite magma
1182 during anatexis of semi-pelitic metasedimentary rocks: an example from St. Malo,
1183 France. J. Petrol. 42, 487-505.

1184 Montel, J.M., Foret, S., Veschambre, M., Nicollet, C., Provost, A., 1996. Electron microprobe
1185 dating of monazite. Chem. Geol. 131, 37-53.

1186 Mulder, J.A., Halpin, J.A., Daczko, N.R., Orth, K., Meffre, S., Thompson, J.M., Morrissey, L.J.,
1187 2019. A multiproxy provenance approach to uncovering the assembly of East Gondwana in
1188 Antarctica. Geology 47, 645-649.

1189 Myers, J.S., 1990. Precambrian tectonic evolution of part of Gondwana, southwestern
1190 Australia. Geology 18, 537-540.

1191 Nandy, D.R., 2001. Geodynamics of the Northeastern India and the Adjoining Region. Acb
1192 Publishers, Delhi, pp. 209.

1193 Newton, R.C., Charlu, T.V., Kleppa, O.J., 1980. Thermochemistry of the high structural state
1194 plagioclases. Geochim. Cosmochim. Acta. 44, 933-941.

1195 Palin, R.M., Weller, O.M., Waters, D.J., Dyck, B., 2016. Quantifying geological uncertainty in
1196 metamorphic phase equilibria modelling; a Monte Carlo assessment and implications for
1197 tectonic interpretations. Geosci. Front. 7, 591-607.

1198 Passchier, C.W., Trouw, R.A., 2005. Microtectonics. Springer Berlin, Heidelberg, pp. 366.

1199 Patiño Douce, A.E., Harris, N., 1998. Experimental constraints on Himalayan anatexis. J.
1200 Petrol. 39(4), 689-710.

1201 Paton, C., Hellstrom, J., Paul, B., Woodhead, J., Hergt, J., 2011. Iolite: Freeware for the
1202 visualisation and processing of mass spectrometric data. J. Analytical At. Spectrom. 26,
1203 2508-2518.

1204 Perchuk, L.L., Aranovich, L.Y., Podlesskii, K.K., Lavrant'eva, I., Gerasimov, V.Y., Fed'Kin,
1205 V.V., Kitsul, V.I., Karsakov, L.P., Berdnikov, N.V., 1985. Precambrian granulites of the
1206 Aldan shield, eastern Siberia, USSR. J. Metamorph. Geol. 3, 265-310.

1207 Pickering, J.M., Johnston, D.A., 1998. Fluid-absent melting behavior of a two-mica metapelite:
1208 experimental constraints on the origin of Black Hills granite. J. Petrol. 39, 1787-1804.

1209 Plavsa, D., Collins, A.S., Foden, J.D., Clark, C., 2015. The evolution of a Gondwanan collisional
1210 orogen: A structural and geochronological appraisal from the Southern Granulite Terrane,
1211 South India. Tectonics. 34, 820-857.

1212 Powell, R., Holland, T.J.B., 2008. On thermobarometry. J. Metamorph. Geol. 26, 155-179.

1213 Prabhakar, N., 2013. Resolving poly-metamorphic Paleoarchean ages by chemical dating of
1214 monazites using multi-spectrometer U, Th and Pb analyses and sub-counting
1215 methodology. Chem. Geol. 347, 255-270.

1216 Putnis, A., 2009. Mineral replacement reactions. Rev. Mineral. Geochem. 70, 87-124.

1217 Rosenberg, C.L., Handy, M.R., 2005. Experimental deformation of partially melted granite
1218 revisited: implications for the continental crust. J. Metamorph. Geol. 23, 19-28.

1219 Rubatto, D., 2002. Zircon trace element geochemistry: partitioning with garnet and the link
1220 between U–Pb ages and metamorphism. Chem. Geol. 184, 123-138.

1221 Rubatto, D., 2017. Zircon: the metamorphic mineral. Rev. Mineral. Geochem. 83, 261-295.

1222 Santosh, M., Tsunogae, T., Malaviarachchi, S.P., Zhang, Z., Ding, H., Tang, L., Dharmapriya,
1223 P.L., 2014. Neoproterozoic crustal evolution in Sri Lanka: insights from petrologic,
1224 geochemical and zircon U–Pb and Lu–Hf isotopic data and implications for Gondwana
1225 assembly. Precambr. Res. 255, 1-29.

1226 Santosh, M., Hu, C.N., He, X.F., Li, S.S., Tsunogae, T., Shaji, E., Indu, G., 2017.
1227 Neoproterozoic arc magmatism in the southern Madurai block, India: Subduction,
1228 relamination, continental outbuilding, and the growth of Gondwana. Gondwana Res. 45, 1-
1229 42.

1230 Sawyer, E.W., 1998. Formation and evolution of granite magmas during crustal reworking: the
1231 significance of diatexites. J. Petrol. 39, 1147-1167.

1232 Sawyer, E.W., 2001. Melt segregation in the continental crust: distribution and movement of
1233 melt in anatectic rocks. J. Metamorph. Geol. 19, 291-309.

1234 Searle, M.P., Cottle, J.M., Streule, M.J., Waters, D.J., 2009. Crustal melt granites and migmatites
1235 along the Himalaya: melt source, segregation, transport and granite emplacement
1236 mechanisms. Earth and Environmental Science Transactions of the Royal Society of
1237 Edinburgh. 100, 219-233.

1238 Sheikh, J.M., Patel, S.C., Champati, A.K., Madhavan, K., Behera, D., Naik, A., Gerdes, A.,
1239 2020. Nepheline syenite intrusions from the Rengali Province, eastern India: Integrating
1240 geological setting, microstructures, and geochronological observations on their syntectonic
1241 emplacement. Precambr. Res. 346, 105802.

Sorcar, N., Hoppe, U., Dasgupta, S., Chakraborty, S., 2014. High-temperature cooling histories of migmatites from the High Himalayan Crystallines in Sikkim, India: rapid cooling unrelated to exhumation?. Contrib. Mineral. Petrol. 167, 1-34.

Spear, F.S., Florence, F.P., 1992. Thermobarometry in granulites: pitfalls and new approaches. Precambr. Res. 55, 209-241.

Spear, F.S., Pyle, J.M., Cherniak, D., 2009. Limitations of chemical dating of monazite. Chem. Geol. 266, 218-230.

Spreitzer, S.K., Walters, J.B., Cruz-Uribe, A., Williams, M.L., Yates, M.G., Jercinovic, M.J., Grew, E.S., Carson, C.J., 2021. Monazite petrochronology of polymetamorphic granulite-facies rocks of the Larsemann Hills, Prydz Bay, East Antarctica. J. Metamorph. Geol. 39, 1205-1228.

Stacey, J.T., Kramers, 1., 1975. Approximation of terrestrial lead isotope evolution by a two-stage model. Earth Planet. Sci. Lett. 26, 207-221.

Stern, R.J., 1994. Arc assembly and continental collision in the Neoproterozoic East African Orogen: implications for the consolidation of Gondwanaland. Annu. Rev. Earth Planet. Sci. 22, 319-351.

Streule, M.J., Searle, M.P., Waters, D.J., Horstwood, M.S., 2010. Metamorphism, melting, and channel flow in the Greater Himalayan Sequence and Makalu leucogranite: Constraints from thermobarometry, metamorphic modeling, and U-Pb geochronology. Tectonics 29, TC5011.

Stüwe, K., 2002. Geodynamics of the Lithosphere. Springer Berlin, pp. 449.

Suzuki, K., Adachi, M., 1991. The chemical Th-U-total Pb isochron ages of zircon and monazite from the Gray Granite of the Hida terrane, Japan. Earth Sci., Nagoya Univ. 38, 11-37.

Suzuki, K., Kato, T., 2008. CHIME dating of monazite, xenotime, zircon and polycrase: Protocol, pitfalls and chemical criterion of possibly discordant age data. Gondwana Res. 14, 569-586.

Tong, L., Liu, Z., Li, Z.X., Liu, X., Zhou, X., 2019. Poly-phase metamorphism of garnet-bearing mafic granulite from the Larsemann Hills, East Antarctica: PT path, U-Pb ages and tectonic implications. Precambr. Res. 326, 385-398.

Vermeesch, P., 2018. IsoplotR: A free and open toolbox for geochronology. Geosci. Front. 9, 1479-1493.

Vernon, R.H., Clarke, G.L., 2008. Principles of Metamorphic Petrology. Cambridge University Press, pp. 478.

Vielzeuf, D., 1983. The spinel and quartz associations in high-grade xenoliths from Tallante (SE Spain) and their potential use in geothermometry and barometry. Contrib. Mineral. Petrol. 82, 301-311.

Waldbaum, D.R., Thompson Jr., J.B., 1968. Mixing properties of sanidine crystalline solutions: II. Calculations based on volume data. American Mineralogist: J. Earth Planet. Mat. 53, 2000-2017.

Wang, W., Zhao, Y., Wei, C., Daczko, N.R., Liu, X., Xiao, W., Zhang, Z., 2022. High-ultrahigh temperature metamorphism in the Larsemann Hills: insights into the tectono-thermal evolution of the Prydz Bay Region, East Antarctica. J. Petrol. 63, egac002.

Wang, Y., Liu, D., Chung, S.L., Tong, L., Ren, L., 2008. SHRIMP zircon age constraints from the Larsemann Hills region, Prydz Bay, for a late Mesoproterozoic to early Neoproterozoic tectono-thermal event in East Antarctica. Am. J. Sci. 308, 573-617.

Wang, X.L., Coble, M.A., Valley, J.W., Shu, X.J., Kitajima, K., Spicuzza, M.J., Sun, T., 2014. Influence of radiation damage on Late Jurassic zircon from southern China: Evidence from in situ measurements of oxygen isotopes, laser Raman, U–Pb ages, and trace elements. Chem. Geol. 389, 122-36.

White, R.W., Powell, R., Clarke, G.L., 2002. The interpretation of reaction textures in Fe-rich metapelitic granulites of the Musgrave Block, central Australia: constraints from mineral equilibria calculations in the system K_2O–FeO–MgO–Al_2O_3–SiO_2–H_2O–TiO_2–Fe_2O_3. J. Metamorph. Geol. 20, 41-55.

White, R.W., Powell, R., Halpin, J.A., 2004. Spatially-focussed melt formation in aluminous metapelites from Broken Hill, Australia. J. Metamorph. Geol. 22, 825-845.

White, R.W., Powell, R., Johnson, T.E., 2014. The effect of Mn on mineral stability in metapelites revisited: New a–x relations for manganese-bearing minerals. J. Metamorph. Geol. 32, 809-828.

Whitney, D.L., Evans, B.W., 2010. Abbreviations for names of rock-forming minerals. Am. Mineral. 95, 185-187.

Whitney, D.L., Teyssier, C., Fayon, A.K., 2004. Isothermal decompression, partial melting and exhumation of deep continental crust. Geol. Soc. London Spec. Publ. 227, 313-326.

Williams, I.S., Claesson, S., 1987. Isotopic evidence for the Precambrian provenance and Caledonian metamorphism of high grade paragneisses from the Seve Nappes, Scandinavian Caledonides: II. Ion microprobe zircon U-Th-Pb. Contrib. Mineral. Petrol. 97, 205-217.

Williams, M.L., Jercinovic, M.J., Goncalves, P., Mahan, K., 2006. Format and philosophy for collecting, compiling, and reporting microprobe monazite ages. Chem. Geol. 225, 1-15.

Wu, C.M., Zhang, J., Ren, L.D., 2004. Empirical garnet–biotite–plagioclase–quartz (GBPQ) geobarometry in medium-to high-grade metapelites. J. Petrol. 45, 1907-1921.

Wu, C.M., 2017. Calibration of the garnet–biotite–Al_2SiO_5–quartz geobarometer for metapelites. J. Metamorph. Geol. 35, 983-998.

Xing, L., Trail, D., Watson, E.B., 2013. Th and U partitioning between monazite and felsic melt. Chem. Geol. 358, 46-53.

Yakymchuk, C., Kirkland, C.L., Clark, C., 2018. Th/U ratios in metamorphic zircon. J. Metamorph. Geol. 36, 715-737.

Yin, A., Dubey, C.S., Webb, A.A.G., Kelty, T.K., Grove, M., Gehrels, G.E., Burgess, W.P., 2010. Geologic correlation of the Himalayan orogen and Indian craton: Part 1. Structural geology, U-Pb zircon geochronology, and tectonic evolution of the Shillong Plateau and its neighboring regions in NE India. Geol. Soc. Am. Bull. 122, 336-359.

Zi, J.W., Muhling, J.R., Rasmussen, B., 2023. Geochemistry of low-temperature (< 350° C) metamorphic and hydrothermal monazite. Earth-Sci. Rev. 249, 104668.

Zong, S., Ren, L., Wu, M., 2021. Grenville-age metamorphism in the Larsemann Hills: PT evolution of the felsic orthogneiss in the Broknes Peninsula, East Antarctica. Int. Geol. Rev. 63, 866-881.

1328

1329 **Figure captions**

1330 **Figure 1:** (a) Paleogeographic reconstruction of Indian shield–Western Australia–East Antarctic
1331 shield during the Late Neoproterozoic to Early Paleozoic Era (800–500 Ma) in the Gondwana
1332 supercontinent assembly (after Gray et al., 2008; Meert and Lieberman, 2008). The acronyms are
1333 ADFB: Aravalli-Delhi Fold Belt; BKC-Bundelkhand Craton; VB-Vindhyan Basin; CITZ-Central
1334 Indian Tectonic Zone; CGB-Chhattisgarh Basin; CGC-Chotanagpur Gneissic Complex; SC-
1335 Singhbhum Craton; EGB-Eastern Ghats Belt; CB-Cuddapah Basin; DC-Dharwar Craton; BC-
1336 Bastar Craton; SGT-Southern Granulite Terrain; NC-Napier Complex; OG-Oygarden Group;
1337 RC-Rayner Complex; CL- Coats Land; DG-Denman Glacier; AFO-Albany–Fraser orogen. (b)
1338 Generalized geological map showing the location of Mikir Hills (red box) in the Assam-
1339 Meghalaya gneissic complex (AMGC; adapted from Bhukosh, Geological Survey of India). The
1340 possible western extent of the Pan-African suture in AMGC is shown for reference (blue-dashed
1341 line; Chatterjee et al., 2007). The inset map indicates the simplified geological map of India,
1342 showing various tectonic subdivisions (Dey et al., 2019), including AMGC. The map also shows
1343 the published age data reported from different gneisses of the AMGC (1-Chatterjee et al., 2007;
1344 2-Chatterjee et al., 2011; 3-Borah et al., 2019; 4-Majumdar and Dutta, 2016).

1345

1346 **Figure 2:** (a) Generalized geological map showing lithological variation in the Mikir Hills
1347 region (Geological Survey of India quadrangle map 83F). The pelitic and quartzo-feldspathic
1348 gneisses investigated in this study were collected from southwestern and northeastern parts (blue
1349 boxes) of the Mikir Hills region, respectively. Published age data reported from different
1350 granitoids of the Mikir Hills (1-Gogoi et al., 2019; 2- Kumar et al., 2017) are shown on the map.
1351 (b–c) Geological maps of the southwestern and northeastern Mikir Hills summarize mesoscopic
1352 structural patterns from migmatised pelitic gneisses, quartzo-feldspathic gneisses and foliated
1353 granites. Stereographic projections of penetrative foliation (gneissosity) suggest that both
1354 gneisses preserve similar structural patterns. However, the southwestern part is characterized by
1355 gently dipping (< 30°) S_2 gneissosity and the northeastern part is dominated by steeply dipping
1356 S_3 gneissic foliation. The pelitic and quartzo-feldspathic gneisses show pervasive gently-dipping
1357 (< 30°) gneissic foliation (S_2) that was folded to develop spaced (weakly-developed) axial planar
1358 foliation (S_3).

1359

1360 **Figure 3:** Field photographs showing the general appearance and structural relations of
1361 migmatised (a–c) pelitic gneisses, (d) quartzo-feldspathic gneisses and (e) foliated granite in the
1362 southwestern Mikir Hills region. The polished slabs (b, c) of pelitic gneisses (samples G52 and
1363 53) show distinct gneissic banding and numerous garnet porphyroblasts. Both gneisses have
1364 undergone extensive partial melting by developing alternate leucocratic and melanocratic layers.
1365 Garnet porphyroblasts are mostly developed in leucocratic layers. (f–i) Field photographs
1366 showing mesoscale structures from quartzo-feldspathic gneisses in the northeastern Mikir Hills
1367 region. The early foliation (S_1) is preserved as interfolial tight to isoclinal folds within the S_2

gneissosity. The shallow plunging folds on S_2 foliation develop penetrative S_3 foliation in northeastern Mikir Hills. Mineral abbreviations are after Whitney and Evans (2010).

Figure 4: X-ray element maps, microphotographs and back-scattered electron (BSE) images showing textural characteristics and mineral assemblages of migmatised pelitic gneisses (a–i) G52 and (j–m) G53. (a) XMapTools produced a thin section scale mosaic showing the typical mineral assemblage in sample G52. (b) Garnet core shows curved inclusion trails of quartz, biotite (Bt_1), ilmenite and rutile, and the rim parts of garnet are devoid of inclusion trails (Supplementary Data Table S1). (c) Growth of garnet porphyroblast with large inclusions of plagioclase (Pl_1) and quartz, indicating that garnet porphyroblasts formed in a matrix composed of biotite (Bt_2) + plagioclase (Pl_2) + quartz + ilmenite + rutile. (d) Thin films of quartz, wetting the grain margins of garnet, indicate the presence of melt in the sample. (e–f) The melt layers in pelitic gneisses show lensoidal sillimanite (Sil_1) aggregates rimmed by plagioclase (Pl_3) and K-feldspar (in set image in 'e'). In addition, fine-grained sillimanite grains (Sil_2) have overgrown garnet rims and matrix biotite grains. (g–h) Cordierite grains are developed within pressure shadow zones of garnet and appear to have formed due to the breakdown of garnet. (i) Garnet porphyroblast showing inclusions of biotite (Bt_1), plagioclase (Pl_1), quartz and ilmenite. (j) Locally, intergrowth texture between cordierite and spinel is observed, indicating the breakdown of garnet. (k) XMapTools produced a thin-section mosaic showing the typical mineral assemblage in sample G53. (l–m) Inclusion-poor garnet porphyroblasts formed within the matrix comprise plagioclase (Pl_2), quartz, biotite and ilmenite. Sillimanite grains (Sil_1) are developed within the matrix minerals and oriented along the foliation. The thin films of quartz wetting the grain boundaries of garnet indicate melting signatures in sample G53. Mineral abbreviations are from Whitney and Evans (2010).

Figure 5: X-ray element maps, microphotographs and back-scattered electron (BSE) images showing textural characteristics and mineral assemblages of migmatised quartzo-feldspathic gneisses (G54 and G55). (a–b) XMapTools produced a thin section scale mosaic showing typical mineral assemblage in samples G55 and G54. (c–e) These gneisses comprise euhedral to subhedral aggregates of garnet porphyroblasts, K-feldspar, plagioclase, quartz, ilmenite and biotite. Mineral abbreviations are from Whitney and Evans (2010).

Figure 6: Garnet X-ray element maps and compositional profiles from (a–b) migmatised pelitic gneisses (G52 and G53) and (c) migmatised quartzo-feldspathic gneiss (G55). Zoning profiles in pelitic gneisses (A–B and C–D) show an increase in X_{Alm} and a decrease in X_{Prp} and X_{Grs} from core to rim. In contrast, garnet porphyroblasts in quartzo-feldspathic gneiss (E–F) show a more or less homogeneous composition, with a slight decrease in X_{Mg} content towards garnet rims.

Figure 7: Triangular diagrams of (a) pyrope–almandine–(spessartine+grossular) (Mange and Morton, 2007) and (b) orthoclase–anorthite–albite (Deer et al., 1992) showing compositional

variations in garnet and feldspar minerals, respectively. (c) X_{Mg} vs Ti (pfu) and X_{Mg} vs Al^{IV} binary diagrams show biotite compositional variations for the samples G52, G53, G54 and G55. Pfu: per formula unit.

Figure 8: A schematic diagram summarizing mineral growth and their compositional variation during different deformation and metamorphic stages observed in (a) migmatised pelitic gneisses (samples G52 and G53) and (b) quartzo-feldspathic gneisses (samples G54 and G55). Abbreviations: M_{PR}-prograde; M_P-peak; M_{PP}-post-peak. Mineral abbreviations are from Whitney and Evans (2010).

Figure 9: MnNCKFMASHTO pseudosections constructed for migmatised pelitic gneisses (a–b) G52 and (c–d) G53 using the Perple_X software program (version 6.9.1). In Figures (a) and (c), residual bulk compositions, measured based on modal abundance, have been used for pseudosection modelling. The intersection (yellow field) of garnet (X_{Alm}, X_{Prp} and X_{Grs}), matrix biotite (X_{Fe}) and plagioclase (Pl_2; X_{Ab}) is used to determine peak *P–T* conditions, whereas garnet (X_{Alm}, X_{Prp} and X_{Grs}) and cordierite (X_{Fe}) compositions are used for estimating post-peak metamorphic conditions. The thick, bold lines connecting the peak and post-peak metamorphic conditions suggest decompression *P–T* paths for the pelitic gneisses. The melt-reintegrated pseudosections were utilized to identify possible prograde paths for the studied samples. For sample G52, the melt-reintegrated pseudosections were constructed after adding 6 vol.%, 12 vol.% and 18 vol.% (three stages) of melts to the measured bulk composition. Similarly, 6 vol.% and 12 vol.% (two stages) of melts were added to sample G53. The dashed grey arrows in figures (b) and (d) represent a possible prograde heating path for the samples G52 and G53. The red stars indicate the positions where melt was reintegrated to the system, and the vertical panels (white lines) represent the pseudosection fields with various proportions of reintegrated melts. Thick red and purple lines indicate melt-in and cordierite-in stability fields, respectively. All mineral abbreviations are after Whitney and Evans (2010).

Figure 10: MnNCKFMASHTO pseudosection constructed for the migmatised quartzo-feldspathic gneiss (G55) using the measured bulk composition. The intersection (yellow field) of garnet (X_{Alm}, X_{Prp} and X_{Grs}), matrix biotite (X_{Fe}) and plagioclase (X_{Ab}) isopleth compositions determines the peak *P–T* conditions. Thick red and purple lines indicate melt-in and muscovite-out stability fields, respectively. The dashed arrow represents the possible *P–T* path, connecting the melt-bearing field and garnet-stabilised peak metamorphic conditions. All mineral abbreviations are after Whitney and Evans (2010).

Figure 11: Representative cathodoluminescence (CL) images and Wetherill plots showing zoning patterns and age distribution of zircon grains, respectively, from (a) migmatised pelitic gneiss (G53) and (b) migmatised quartzo-feldspathic gneiss (G55). Zircon grains are shown with

analyzed spots (25 μm) and the corresponding $^{207}Pb/^{206}Pb$ dates (±2σ errors). In the Concordia plots, the number of data points considered for age calculation is indicated with '*n*'. The upper intercept (UI) and lower intercept (LI) age values and corresponding MSWD values are shown. The green-filled and grey ellipses represent data points considered for age calculation and discarded data points, respectively.

Figure 12: Back-scattered electron images, X-ray element maps and probability density plots showing textural occurrence, compositional variations and age distribution of monazites, respectively, from (a–f) migmatised pelitic gneisses (G53 and G52) and (g–l) migmatised quartzo-feldspathic gneisses (G55 and G54). Monazite X-ray elements maps are marked with individual spot ages (±2σ), whereas probability density plots are shown with weighted mean ages (±2σ). In addition, compositional domains identified for different pelitic (CD_P1 and CD_P2) and quartzo-feldspathic (CD_Q1 and CD_Q2) gneisses are shown. Mineral abbreviations are after Whitney and Evans (2010).

Figure 13: (a) Pressure-temperature diagram showing a summary of *P–T* paths obtained for the pelitic gneisses (G53, pink line; G52, blue line) and quartzo-feldspathic gneiss (G55; green line). The diagram also shows a schematic representation of mineral growth during prograde, peak and post-peak metamorphic episodes. (b) The P –T paths obtained in this study are correlated with the Late Cambrian to Ordovician metamorphic *P–T* paths derived from rocks of the central AMGC (NE India; blue lines) and Prydz Bay (East Antarctica; black lines) regions. Central AMGC: AM1–Umpretha metapelites (Chatterjee et al., 2007); AM2–Sonapahar metapelites (Dwivedi et al., 2020). Prydz bay: 1–Grove Mountains Mafic granulites (Liu et al., 2009); 2–Grove mountains metapelites (Chen et al., 2018); 3–Pelitic and mafic granulite of Larsemann Hills (Carson et al., 1997); 4–Mather paragneiss from Rauer Group (Kelsey et al., 2007); 5–UHT granulites from Larsemann Hills (Wang et al., 2022), 6–Brattstrand Bluffs paragneiss (Fitzsimons, 1996). *P–T* ranges of different metamorphic facies are given after Stüwe (2002). Thermal gradients are adapted from Kelsey and Hand (2015). Abbreviations: AF–Amphibolite facies; GR–Granulite facies; UHT–Ultra-High temperature facies; HGR–High-P granulite facies. (c–e) Summary of zircon and monazite ages obtained from eastern, central and western parts of the Assam-Meghalaya Gneissic Complex. The peak ages (dashed lines; in Ma) shown on the diagrams are considered from probability density plots. Horizontal bars shown in (a) and (b) represent the age ranges of three major episodes (1700–1470 Ma, 1150–980 Ma and 560–420 Ma) of granite magmatism in the Assam-Meghalaya Gneissic Complex. (*)U-Th-total Pb monazite ages are compiled from Chatterjee et al. (2007, 2011), Chatterjee (2017), Borah et al. (2019) and Dwivedi et al. (2020).

Figure 14: (a) A schematic diagram (not to scale) illustrating the tectonic-metamorphic evolution of AMGC (including Mikir Hills) during ~1100–1000 Ma and ~550–450 Ma. The tectonic scenario between India and Antarctica during ~1100–1000 Ma is adopted from Bose et al. (2022). Abbreviations: BC-Bastar Craton, DC-Dharwar Craton, SC-Singhbhum Craton,

AMGC-Assam-Meghalaya Gneissic Complex. The contractional deformation at ~550–450 Ma led to crustal thickening associated with the collision between India-Australia-Antarctica cratons. At this stage, magmatic underplating beneath the Mesoproterozoic crust resulted in prograde partial melting of pelitic and quartzo-feldspathic gneisses (M_{PR} to M_P), followed by isothermal decompression event (M_P to M_{PP}) during orogenic collapse. This high-grade metamorphic episode is contemporary with the emplacement of post-collisional A-type granitoids in the AMGC, including the Mikir Hills region (Majumdar and Dutta, 2016). (b) The schematic diagram showing the correlation of magmato-metamorphic events among Assam-Meghalaya Gneissic Complex (AMGC, northeast India), Western Australia and Prydz Bay (East Antarctica). References (AMGC): [1] Kumar et al., 2017; [2] Majumdar and Dutta, 2016; [3] Chatterjee et al., 2007; [4] Chatterjee et al., 2011; [5] Dwivedi et al., 2020; [6] Yin et al., 2010; [7] Gogoi et al., 2019; References (Western Australia): [i] Collins, 2003; [ii] Markwitz et al., 2017; [iii] Boger, 2011; [iv] Bruguier et al., 1999; References (Prydz Bay): [a] Spreitzer et al., 2021; [b] Matthews, 2013; [c] Grew et al., 2012; [d] Wang et al., 2008; [e] Tong et al., 2019; [f] Zong et al., 2021; [g] Liu et al., 2009.

Table captions

Table 1: Lithology, sample locations and mineral assemblages of investigated samples in the Mikir Hills.

Table 2: Calculated modal abundances (vol.%) of various minerals in migmatised pelitic gneisses (G52 and G53) and quartzo-feldspathic gneisses (G54 and G55) using the XMapTools program.

Table 3: Summary of conventional thermobarometry results obtained for pelitic gneisses (G53 and G52) and quartzo-feldspathic gneiss (G55) of the Mikir Hills.

Table 4: Whole rock compositions (in wt.%) of migmatised pelitic gneiss (G52 and G53) and quartzo-feldspathic gneiss (G55) along with normalized bulk compositions and melt-reintegrated bulk compositions (mol.%) used for phase equilibrium modelling.

Table 5: Summary of zoning patterns, textural setting, compositional variations and age ranges obtained for zircon (G53 and G55) and monazite (G52, G53, G54 and G55) grains from pelitic and quartzo-feldspathic gneisses.

Supplementary Figure captions

Figure S1: MnNCKFMASHTO pseudosections constructed for pelitic gneiss samples (a–c) G52 and (d–e) G53 after different stages of melt-reintegration.

Figure S2: (a) Age vs. LREE, (b) age vs. Th/U, (c) age vs. HREE and (d) chondrite-normalized (McDonough and Sun, 1995) plot showing chemical composition variation of different compositional domains in migmatised pelitic and quartzo-feldspathic gneisses. (e–f) ThO_2* (ThO_2 plus the equivalent of UO_2) vs. PbO plots showing chemical isochron ages for different monazite compositional domains. The errors in the figure represent 2σ analytical uncertainty.

Supplementary Table Captions

Table S1: Detailed compositions and structural formulae of the various minerals in migmatised pelitic gneisses (G53 and 52) and quartzo-feldspathic gneisses (G54 and 55).

Table S2: Analytical conditions for LA-ICP-MS zircon dating.

Table S3: Summary of LA-ICPMS analyzed U–Pb zircon isotope ratios and dates (in Ma) for pelitic gneiss (G53), quartzo-feldspathic gneiss (G55) and zircon standard (GJ1).

Table S4: Monazite trace element data (in wt.%) and corresponding U–Th–total Pb ages (in Ma) obtained for migmatised pelitic gneisses (G53 and 52) and quartzo-feldspathic gneisses (G54 and 55).

Highlights

- Mikir Hills form part of the Kuunga orogen during the final assembly of Gondwana
- Gneisses of Mikir Hills preserve high-grade metamorphism and migmatisation.
- *P–T* estimates suggest a clockwise *P–T* history with isothermal decompression path.
- Zircons inherited Mesoproterozoic protolith ages 1647 ± 11 Ma and 1590 ± 7 Ma.
- Monazite dating reveals the timing of migmatisation at 496 ± 7 Ma to 467 ± 16 Ma.

Table 1: Lithology, sample locations and mineral assemblages of investigated samples in the Mikir Hills

S. No.	Rock type (sample number)	Lat/long	Mineral assemblage
1	Migmatised pelitic gneiss (G52)	26°09.540' 93°09.910'	Garnet + Cordierite + Sillimanite + K-feldspar + Plagioclase + Biotite + Spinel + Quartz + Ilmenite + Rutile + Monazite + Zircon
2	Migmatised pelitic gneiss (G53)	26°09.350' 93°09.970'	Garnet + Cordierite + Sillimanite + K-feldspar + Plagioclase + Biotite + Quartz + Ilmenite + Rutile + Monazite + Zircon
3	Migmatised quartzo-feldspathic gneiss (G55)	26°32.423' 93°42.292'	Garnet + K-feldspar + Plagioclase + Biotite + Quartz + Ilmenite + Magnetite + Monazite + Zircon
4	Migmatised quartzo-feldspathic gneiss (G54)	26°33.893' 93°41.319'	Garnet + K-feldspar + Plagioclase + Biotite + Quartz + Ilmenite + Chlorite + Muscovite + Monazite + Zircon

1553

1554

1555 **Table 2:** Calculated modal abundances (vol.%) of various minerals in migmatised pelitic
1556 gneisses (G52 and G53) and quartzo-feldspathic gneisses (G54 and G55) using the XMapTools
1557 program.

Sample No.	G53	G52	G55	G54
Garnet	5.05	13.53	0.42	0.20
Plagioclase		18.21	34.69	25.87

Ilmenite	0.86	1.19	0.73	0.08
Biotite	8.46	5.87	1.99	2.77
K-feldspar	12.58	15.98	8.82	24.27
Quartz	45.89	31.68	33.39	28.54
Sillimanite	4.15	4.77	--	--
Cordierite	15.84	7.42	--	--
Rutile	0.04	0.05	--	--

1558

1559

1560

1561

1562

1563

1564

1565

1566

Table 3: Summary of conventional thermobarometry results obtained for pelitic gneisses (G53 and 52) and quartzofeldspathic gneiss (G55) of the Mikir Hills.

Metamorphic events	**Rock types (sample no.)**	**Mineral pairs used**	**Mineral equilibria used for thermobarometry and Calibrations**	**T (°C)**	**P (kbar)**

Peak (M_P)	G52 (Migmatised pelitic gneisses)	Grt(core)-Bt_2	Grt-Bt thermometry (Holdaway, 2000)	700–753	-
		Grt(core)-Bt_2-Pl_2	GB-GASP thermobarometry (Ganguly et al., 1996)	674–778	4.92–6.59
		Bt_2	Ti-in-Biotite thermometry (Henry et al., 2005)	740–777	-
		Grt(core)-Bt_2-Pl_2	Grt-Bt-Pl-Qz barometer (Wu et al., 2004)	-	7.52–8.42
		Grt(core)-Bt_2	Grt-Bt-Als-Qz barometer (Wu et al., 2017)	-	4.79–5.72
	G53 (Migmatised pelitic gneisses)	Grt(core)-Bt_2	Grt-Bt thermometry (Holdaway, 2000)	620–673	-
		Grt(core)-Bt_2-Pl_2	GB-GASP thermobarometry (Ganguly et al., 1996)	636–767	4.23–5.56
		Bt_2	Ti-in-Biotite thermometry (Henry et al., 2005)	645–728	-
		Grt(core)-Bt_2-Pl_2	Grt-Bt-Pl-Qz barometer (Wu et al., 2004)	-	5.70–7.37
		Grt(core)-Bt_2	Grt-Bt-Als-Qz barometer (Wu et al., 2017)	-	5.68–6.43
	G55 (Migmatised quartzo-feldspathic gneisses)	Grt(core)-Bt	Grt-Bt thermometry (Holdaway, 2000)	601–618	-
		Grt(core)-Bt-Pl	GB-GASP thermobarometry (Ganguly et al., 1996)	496–531	-
		Bt	Ti-in-Biotite thermometry (Henry et al., 2005)	625–658	-

		Grt(core)-Bt-Pl	Grt-Bt-Pl-Qz barometer (Wu et al., 2004)	-	6.66–7.44
Post-peak (M_{PP})	G52 (Migmatised pelitic gneisses)	Grt(rim)-Bt_2 (attached to Grt)	Grt-Bt thermometry (Holdaway, 2000)	611–658	-
		Grt(rim)-Bt_2 (attached to Grt)	Grt-Bt thermometry (Ganguly et al., 1996)	563–660	-
		Grt(rim)-Crd(rim)	Grt-Crd thermometry (Bhattacharya et al., 1988)	670–708	-
		Spl-Crd	Spl-Crd thermometry (Vielzeuf, 1983)	667–720	-
		Bt_2 (attached to Grt)	Ti-in-Biotite thermometry (Henry et al., 2005)	715–759	-
		Grt(rim)-Bt_2 (attached to Grt)	Grt-Bt-Als-Qz barometer (Wu et al., 2017)	-	2.14–2.52
		Grt(rim)-Crd(rim)	Grt-Crd-Sil-Qz (Perchuk et al., 1985)	-	4.14–4.43
	G53 (Migmatised pelitic gneisses)	Grt(rim)-Bt_2 (attached to Grt)	Grt-Bt thermometry (Holdaway, 2000)	552–564	-
		Grt(rim)-Bt_2 (attached to Grt)	Grt-Bt thermometry (Ganguly et al., 1996)	495–583	-
		Grt(rim)-Crd(rim)	Grt-Crd thermometry (Bhattacharya et al., 1988)	564–599	-

		Bt_2 (attached to Grt)	Ti-in-Biotite thermometry (Henry et al., 2005)	645–676	-
		Grt(rim)-Bt_2 (attached to Grt)	Grt-Bt-Als-Qz barometer (Wu et al., 2017)	-	2.45–2.71
		Grt(rim)-Crd(rim)	Grt-Crd-Sil-Qz (Perchuk et al., 1985)	-	2.34–2.75

1567

1568

1569

Table 4: Whole rock compositions (in wt.%) of migmatised pelitic gneiss (G52 and G53) and quartzo-feldspathic gneiss (G55) along with normalised bulk compositions and melt-reintegrated bulk compositions (mol.%) used for phase equilibrium modelling.

S. No.	Whole rock composition (in wt.%)												
	Sample			SiO_2	Al_2O_3	FeO	MnO	MgO	CaO	Na_2O	TiO_2	K_2O	H_2O	O_2	Total
	G52			59.80	22.29	8.99	0.09	2.13	1.29	1.58	1.29	2.33	0.24	0.04	100.03
1	Normalised molar propotion														
	Sample	Stage of melt reintegration	Figure	SiO_2	Al_2O_3	FeO	MnO	MgO	CaO	Na_2O	TiO_2	K_2O	H_2O	O_2	Total
	G52	Residual	Fig. 8a	66.48	14.60	8.36	0.08	3.53	1.54	1.70	1.08	1.65	0.89	0.08	100.00

	1st stage	Fig. 8b	66.48	14.28	7.94	0.08	3.35	1.49	1.81	0.57	1.73	2.20	0.07	100.00
	2nd stage	Fig. 8b	66.05	13.89	7.50	0.07	3.16	1.43	1.90	0.54	1.79	3.59	0.07	100.00
	3rd stage	Fig. 8b	65.45	13.48	7.08	0.07	3.00	1.37	2.01	0.51	1.80	5.17	0.06	100.00

Whole rock composition (in wt.%)

	Sample	Details	SiO_2	Al_2O_3	FeO	MnO	MgO	CaO	Na_2O	TiO_2	K_2O	H_2O	O_2	Total
	G53		62.65	16.95	6.59	0.09	0.97	0.97	2.75	0.83	7.67	0.51	0.04	100.02

Normalised molar propotion

2	Sample	Stage of melt reintegration	Figure	SiO_2	Al_2O_3	FeO	MnO	MgO	CaO	Na_2O	TiO_2	K_2O	H_2O	O_2	Total
		Residual	Fig. 8c	69.11	11.02	6.08	0.08	1.60	1.15	2.94	0.69	5.39	1.87	0.07	100.00
	G53	1st stage	Fig. 8d	68.56	10.81	5.75	0.08	1.51	1.10	2.97	0.65	5.25	3.27	0.07	100.00
		2nd stage	Fig. 8d	67.86	10.58	5.43	0.07	1.42	1.05	3.00	0.61	5.09	4.82	0.06	100.00

Whole rock composition (in wt.%)

Sample			SiO_2	Al_2O_3	FeO	MnO	MgO	CaO	Na_2O	TiO_2	K_2O	H_2O	O_2	Total
G55			77.18	12.19	2.06	0.62	0.32	1.18	4.60	0.79	2.03	0.12	0.04	101.09
			Normalised molar propotion											
Sample	Stage of melt reintegration	Figure	SiO_2	Al_2O_3	FeO	MnO	MgO	CaO	Na_2O	TiO_2	K_2O	H_2O	O_2	Total
G55	Residual	Fig. 9a, b	81.09	7.55	1.81	0.55	0.50	1.32	4.69	0.62	1.36	0.42	0.08	100.00

3

1570

1571

Table 5: Summary of zoning patterns, textural setting, compositional variations and age ranges obtained from zircon (G53 and G55) and monazite (G52, G53, G54 and G55) grains of pelitic and quartzo-feldspathic gneisses.

U-Pb zircon dating

Lithology	**Zoning pattern in zircons**	**Th/U ratios**	**Concordant and discordant ages (in Ma) (±2σ)**
G53: Migmatised pelitic gneiss	Bright-CL oscillatory growth zones rimmed by dark-CL metamorphic recrystallization rims; bright-CL xenocrystic core surrounded by dark-CL oscillatory zoning pattern; Oscillatory zoning surrounded by patchy zoning which is further rimmed by bright-CL recrystallization rims	0.59–1.01	Concordant age: 1647 ± 11 (±16) Ma (n = 3; MSWD = 1.3); Discordia age: Upper intercept 1683 ± 44 (±45) Ma (n = 13, MSWD = 1.4)

G55: Migmatised quartzo-feldspathicgneiss	Dark-CL xenocrystic cores surrounded by oscillatory zoning pattern; Oscillatory zoning pattern surrounded by bright-CL recrystallization rims; bright-CL patchy zoning surrounded by dark-CL oscillatory zoning pattern; Metamictized core surrounded by oscillatory zoning pattern	0.77–1.82	Concordant age: 1590 ± 7 (±14) Ma (n = 6; MSWD = 1.0); Discordia age: Upper intercept 1613 ± 19 (±22) Ma (n = 16; MSWD = 1.3)
U-Th-(total) Pb monazite dating			
Lithology	**Textural setting**	**Compositional variations (in wt.%)**	**U-Th-Pb(total) ages (±2σ)**
G53: Migmatised pelitic gneiss	Medium sized (~100 µm to ~200 µm; long axis), subrounded to rounded and subhedral to anhedral prismatic grains occurring as inclusions within shape-preferred biotite and in quartz + K-feldspar+ plagioclase matrix	CD_P1: Y_2O_3 = 0.37 to 1.84; ThO_2 = 3.90 to 4.95, UO_2 = 0.24 to 1.08; CD_P2: Y_2O_3 = 0.30 to 2.81; ThO_2 = 4.20 to 5.48; UO_2 = 0.17 to 0.36	CD_P1: 1016 ± 48 Ma to 1112 ± 55 Ma; Mean age: 1058 ± 35 Ma (n=6; MSWD = 1.8); CD_P2: 460 ± 33 Ma to 479 ± 36 Ma; Mean age: 467 ± 16 Ma (n=5; MSWD = 0.24)
G52: Migmatised pelitic gneiss	Medium-to-long prismatic (~50 µm to ~600 µm; long axis), wedge-shaped and ellipsoidal subhedral to anhedral grains) occurring as inclusions within garnet and quartz + K-feldspar+ plagioclase matrix	CD_P2: Y_2O_3 = up to 0.59; ThO_2 = 5.21 to 10.76; UO_2 = 0.11 to 1.62	CD_P2: 450 ± 35 Ma to 530 ± 22 Ma; Mean age: 480 ± 8 Ma (n=31; MSWD = 2.8)
G55: Migmatised quartzo-feldspathicgneiss	Subrounded short-to-medium subhedral to anhedral grains ranging from ~60 µm to ~120 µm (long axis) in size occurring as inclusions within K-feldspar, quartz and biotite in the leucosome part of the rock	CD_Q1: Y_2O_3 = 2.33 to 3.22; ThO_2 = 6.95 to 8.02; UO_2 = 0.09 to 0.36; CD_Q2: Y_2O_3 = 1.98 to 2.49; ThO_2 = 2.92 to 5.36; UO_2 = 0.18 to 0.87	CD_Q1: 455 ± 30 Ma to 478 ± 27 Ma; Mean age: 469 ± 16 Ma (n=3; MSWD = 0.67); CD_Q2: 403 ± 47 Ma to 450 ± 41 Ma; Mean age: 427 ± 17 Ma (n=5; MSWD = 0.74)
	Prismatic subrounded medium to long (~80 µm to ~200 µm;	CD_Q1: Y_2O_3 = 1.69 to 2.90; ThO_2 = 8.71 to 16.85,	CD_Q1: 471 ± 21 Ma to 523 ± 22 Ma; Mean

G54: Migmatised quartzo-feldspathicgneiss	long axis) and subhedral to anhedral grains occurring as inclusions within K-feldspar, plagioclase, quartz and biotite in the matrix	UO_2 = 0.12 to 0.47; CD_Q2: Y_2O_3 = 1.71 to 2.33; ThO_2 = 3.75 to 9.77, UO_2 = 0.06 to 0.39	age: 496 ± 7 Ma (*n*=18; MSWD = 1.4) CD_Q2: 429 ± 28 Ma to 450 ± 34 Ma; Mean age: 439 ± 13 Ma (*n*=5; MSWD = 0.30)

1572

1573